



Exposed H₂O-rich areas detected on Ceres with the dawn visible and infrared mapping spectrometer



Jean-Philippe Combe^{a,*}, Andrea Raponi^b, Federico Tosi^b, Maria Cristina De Sanctis^b, Filippo Giacomo Carrozzo^b, Francesca Zambon^b, Eleonora Ammannito^{b,c,d}, Kynan H.G. Hughson^d, Andreas Nathues^e, Martin Hoffmann^e, Thomas Platz^{e,f}, Guneshwar Thangjam^e, Norbert Schorghofer^f, Stefan Schröder^g, Shane Byrne^h, Margaret E. Landis^h, Ottaviano Rueschⁱ, Thomas B. McCord^a, Katherine E. Johnson^a, Sandeep Magar Singh^a, Carol A. Raymond^j, Christopher T. Russell^d

^a Bear Fight Institute, 22 Fiddler's Road, P.O. Box 667, Winthrop, WA 98862, USA

^b Istituto di Astrofisica e Planetologia Spaziali-Istituto Nazionale di Astrofisica, Rome, Italy

^c Agenzia Spaziale Italiana, Rome, Italy

^d Institute of Geophysics and Planetary Physics, University of California Los Angeles, CA, USA

^e Max Planck Institute for Solar System Research, Planets and Comets Department, 37077 Göttingen, Germany

^f Planetary Science Institute, Tucson, AZ, USA

^g Deutsches Zentrum für Luft- und Raumfahrt, Department German Aerospace Center Institute of Planetary Research, Planetary Geology Rutherfordstraße 2, 12489 Berlin, Germany

^h Lunar and Planetary Laboratory, Tucson, AZ, USA

ⁱ European Space Agency, European Space Research and Technology Centre, Noordwijk, The Netherlands

^j Jet Propulsion Laboratory, Pasadena, CA, USA

ARTICLE INFO

Article history:

Received 26 April 2017

Revised 29 November 2017

Accepted 7 December 2017

Available online 19 December 2017

Keywords:

Dwarf planet Ceres

Surface composition

Exposed H₂O ice

Reflectance spectroscopy

ABSTRACT

H₂O-rich materials are locally exposed at the surface of Ceres as discovered from infrared reflectance spectra of the Visible and InfraRed mapping spectrometer (VIR) of the Dawn mission. Nine locations on Ceres exhibit diagnostic absorption bands of the H₂O molecule at 2.00, 1.65 and 1.28 μm. The detections are all consistent with H₂O ice mixed with low-albedo components. All the reported H₂O exposures occur at latitudes poleward of 30° in fresh craters near rim shadows, have a surface area < 7 km², and are associated with one or more surface features such as a morphological flow or landslide, fractures, high albedo, or a pole-facing slope (one case is confirmed to be adjacent to persistent shadow). In four occurrences, these detections are associated with small (< 0.1 km²) high-albedo areas that can be recognized in high-resolution imagery (~35 m/pixel) from the Framing Camera (FC). Since all these observations are compatible with an H₂O-rich subsurface, the replenishment of surficial H₂O likely comes from the ice that is present underneath. In four other occurrences, H₂O is detected on walls and floors of fresh impact craters, either in the shadow or adjacent to shadows, which suggests that local thermodynamical conditions may also favor the concentration of H₂O in these areas.

© 2018 Elsevier Inc. All rights reserved.

1. Introduction

H₂O is a fundamental component of Ceres, as inferred from almost four decades of ground telescopic observations, geophysical modeling, and two years in orbit by the Dawn mission (Russell and Raymond, 2011). To date, surficial H₂O on Ceres has been detected by Dawn's Visible and InfraRed mapping spectrometer (VIR) in

three fresh impact craters such as Oxo (Combe et al., 2016), a small, unnamed crater at 70°N (Platz et al., 2016; Ermakov et al., 2017), and Juling Crater (Raponi et al., 2018). Further potential ice-rich depositions in permanently shadowed craters have been identified (Platz et al., 2016). In addition, the surface morphology observed at high resolution in images from Dawn's Framing Camera (FC) revealed possible cryovolcanism (Ruesch et al., 2016; Nathues et al., 2017) and flow-like morphological features that could be due to ground H₂O ice (Schmidt et al., 2017). The presence of significant amounts of H₂O is further supported by the inferred upper crust stratigraphy of Ceres (Nathues et al., 2016).

* Corresponding author.

E-mail address: jean-philippe_combe@bearfightinstitute.com (J.-P. Combe).

From Dawn's Gamma-Ray and Neutron Detector (GRaND), hydrogen was detected within 1 m of the subsurface (between 16 and 29 weight % in H₂O-equivalent H), and its distribution is interpreted as a variation of the ice table depth as a function of latitude (Prettyman et al., 2016). Before the Dawn mission, H₂O was inferred to be a likely component from calculation of its mass, size and low bulk density (McCord and Sotin, 2005), its shape that suggested differentiation (Thomas et al., 2005) and from thermo-physical modeling. Thermodynamical models of its internal structure indicated differentiation with amounts of H₂O as high as 26% in the average bulk composition (McCord and Sotin, 2005; Castillo-Rogez and McCord, 2010) and 48–55% in the 70–190 km of its crust (Park et al., 2016). The importance of H₂O in the chemistry of Ceres came from spectral properties in the near-infrared that revealed hydroxylated minerals likely resulting from the aqueous alteration of silicate rocks by water (Lebofsky et al., 1981; Vernazza et al., 2005; Rivkin et al., 2006; Milliken and Rivkin, 2009; De Sanctis et al., 2015; Ammannito et al., 2016). Evidence of transient phenomena was also reported, such as OH fluorescence over the north pole (A'Hearn and Feldman, 1992), the release of H₂O molecules (Küppers et al., 2014), the presence of haze above high-albedo faculae (Nathues et al., 2015; Thangjam et al., 2016), and the temporary acceleration of the solar wind around Ceres that could be explained by a temporary exosphere (Villarreal et al., 2017), although none has reported temporal variations at the surface due to the suggested activity. All of these studies are consistent with the fundamental role of H₂O in the evolution and internal activity of Ceres over geological times that may have led to partial differentiation, the release of H₂O similar to cometary activity, and the cause of possible transient phenomena at the surface in present times.

In this study, we present nine areas where H₂O-rich materials are exposed at the surface of Ceres, resulting from processing the entire VIR IR dataset of the Dawn mission at Ceres from the Approach phase to the end of the Low-Altitude Mapping Orbit phase. Our objective is to determine whether the surficial H₂O on Ceres is the expression of internal activity, or if it results from thermo-physical or mechanical processes of the surface. Meteoroid impacts, landslides, migration of H₂O molecules (Schorghofer et al., 2016), and cryovolcanism (Ruesch et al., 2016; Nathues et al., 2017) exist on Ceres and make the detection of H₂O possible today. Mechanical processes likely occur, as inferred from the discovery of H₂O in the Oxo crater (Combe et al., 2016), which suggests that a recent meteorite impact (less than 10 Ma) and very recent landslides have exposed H₂O from a water-ice rich subsurface (Nathues et al., 2017). The local pole-facing, 20° slope and the proximity of a sharp scarp that casts shadows likely favors the preservation of H₂O ice (Landis et al., 2017). By making an exhaustive inventory of H₂O-rich materials exposed on Ceres, we can gain insight into the distribution, extent, abundance, geological context and thermal conditions of these areas, because the distribution of findings (local or widespread) can be indicative of the origin of surficial H₂O.

Reflectance spectroscopy is the only direct way to identify H₂O exposed at the surface of Ceres with the Dawn mission. As a consequence, a refined analysis of VIR spectra is suited for the finding of more H₂O-rich areas on Ceres. Examination of the morphological and albedo features with high-resolution imagery can help validate and interpret the geological context of any new detection. The methodology of spectral analysis of VIR IR spectra can be adapted to search for weak absorption bands of H₂O in individual spectra spread over a large dataset (several million spectra) in order to optimize the probability of detection. One technique – linear spectral unmixing – is easily reproducible, is fast enough to be manageable for large datasets, and can be fine-tuned for enhanced sensitivity to one or more absorption bands. The processing of remote-sensing spectra implies the selection of one or more reference spectra (spectral endmembers) that is associated with

a known composition. The model finds the linear combination that results in the best fit, and it provides both weighing factors (mixing coefficient) and quality of fit (such as the Root-Mean Squares). Although this technique is primarily designed for the analysis of mixed components, it can also serve the function of spectral feature fitting for the search of specific absorption bands.

In the present study, we search for H₂O-rich materials in multiple areas on Ceres and study its distribution. VIR IR data were processed and analyzed specifically for the search of spectra similar to those of H₂O. All spectra associated to the nine findings of H₂O are consistent with the presence of ice. All areas of exposed H₂O-rich materials are located at latitudes above 30°, seven of them in the northern hemisphere, and two in the southern hemisphere. All H₂O detections are associated with surface albedo properties or morphological features as expected when H₂O is present in the surface material. Specifically, we identified four types of regions, based on the type of albedo or morphological properties.

2. Dawn VIR infrared data and processing methodology

2.1. Instrument and data specifications

For the detection and characterization of H₂O-rich areas on Ceres, we focused on the analysis of spectra from the infrared detector of Dawn's VIR imaging spectrometer (De Sanctis et al., 2011), which is sensitive to the radiation range 1.02–5.10 μm where vibration absorption processes of the H₂O molecule occur. VIR-IR is a push-broom detector constituted of 256 spatial pixels by 432 spectral pixels, with spectral sampling of 9.8 nm, and with an Instantaneous field of View (IFOV) of 250 μrad/pixel.

Dawn began observing Ceres in January 2015. The mission was divided into seven main observational phases (Table 1). Each phase differs in duration, illumination conditions (with the phase angle increasing from Survey to Low-Altitude Mapping Orbit (LAMO)), and surface coverage. Global mapping was achieved by VIR for all latitudes below 70°, with some redundancy; only the polar regions were not observed. We used all VIR IR data available from the beginning of the Dawn mission at Ceres to August 26, 2016, which represents $\sim 28.15 \times 10^6$ spectra in 1772 observation files.

2.2. Calibration improvement

VIR IR level 1b data are already calibrated into radiance ($\text{W}\cdot\text{m}^{-2}\cdot\text{sr}^{-1}\cdot\mu\text{m}^{-1}$), however they are still affected by instrument artifacts such as spikes (usually caused by cosmic rays), a saw-tooth effect in the spectra due to different gains of odd and even wavelength channels, systematic features in the spectra, and systematic vertical stripes in the images before geographical projection. All of these undesired effects can be minimized using threshold values for spike detection, median calculation for spike removal, flat field correction for minimization of systematic spatial artifacts; correction of the instrument responsivity function, and odd-even channel correction based on averaging. All of these calibration steps are described in detail in Combe et al. (2015), except for two of them that are now performed differently: (1) the flat-field correction now relies on the analysis of the entire Vesta and Ceres VIR IR dataset instead of just the Vesta observations, and (2) the instrument responsivity function is adjusted to ground observations (Carrozzo et al., 2016) from the Small Main-Belt Asteroid Spectroscopic Survey (SMASS, Xu et al., 1995).

2.3. Photometric correction

In this study, VIR spectra are calibrated to bidirectional reflectance. First, we calculate the reflectance factor (Hapke, 1981), defined as $I/F \times d^2/\pi$, where I is the irradiance from the surface of

Table 1
Dawn at Ceres mission phases.

Orbit phase	Dates	Altitude (km)	Resolution of FC (m/pixel)	Resolution of VIR (km/pixel)
Approach	December 1, 2014 – April 23, 2015	$1.2e^6$ – $2.2e^4$	$1.12e5$ – $2.1e3$	
RC3	April 23, 2015–May 9, 2015	13,500	1300	~ 3.64
Transfer to Survey				3.64–1.1
Survey	June 6, 2015–June 30, 2015	4400	410	~ 1.1
High-Altitude Mapping Orbit (HAMO)	August 17, 2015–October 23, 2015	1450	140	~ 0.36–0.40
Low-Altitude Mapping Orbit (LAMO)	December 16, 2015–September 2, 2016	375	35	~ 0.09 - 0.1
Extended Juling Orbit (CXJ)	October 5, 2016–November 4, 2016	1450	140	~ 0.36 - 0.40

Ceres that reaches the instrument, F the solar radiant flux, and d is the distance from the Sun to the surface. An accurate estimate of the solar flux at the surface requires measurements of the solar incidence angle at the surface with respect to the topography. Therefore, the conversion from I/F to bidirectional reflectance requires a correction of surface photometric effects, which relies on measurements of the emergence angle with respect to the normal to the surface, and the phase angle. These angles come from evaluation of Ceres' topography, such as the global shape model calculated by [Park et al. \(2016\)](#).

In detail, the correction is performed as follows:

- (1) In order to calculate geographic coordinates, the incidence, emergence and phase angles, we used the standard Navigation and Ancillary Information Facility (NAIF) SPICE system ([Acton, 1996](#)), which contains the attitude and trajectory files of the spacecraft reconstructed a posteriori from telemetry data. For each VIR pixel, we calculated the surface intercept of the line of sight of the IFOV four corners at the beginning and at the end of the data acquisition. The duration of the integration time is important to consider because it accounts for the relative motion of the spacecraft with respect to the surface, and it may eventually represent several times the projected area of the IFOV. More details are provided in [Combe et al. \(2015\)](#).
- (2) A first correction of photometric effects accounts for the topography at scales larger than the size of a VIR pixel projected at the surface. The Ceres shape model ([Park et al., 2016](#)) has higher spatial resolution than VIR, even for LAMO observations. The Akimov disk-function ([Akimov, 1975](#); [Shkuratov et al., 1999](#)) is a model that has been proven to be adequate for the surface of Ceres ([Schröder et al., 2017](#); [Li et al., 2016](#); [Longobardo et al., 2016](#)). It is a scalar multiplied by each VIR I/F spectrum.
- (3) Finally a phase function correction accounts for the physical structure of the surface materials such as surface roughness (performed after correction by the Akimov disk-function). In the case of Ceres, this curve is best fitted by a polynomial function in the logarithmic space. The correction is applied as a vector multiplied to each VIR pixel. We standardize bidirectional reflectances to incidence angles of 0° and emission angles of 30° , which is the common geometry for many laboratory measurements of reflectance spectroscopy (e.g. RELAB, [Pieters, 1983](#)).

2.4. Search for H₂O-rich materials

Our approach consists of scaling and ratioing VIR spectra. For scaling, we divide each spectrum by its median value in the intervals 1.10–1.40 μm and 1.62–2.40 μm . These ranges avoid instrument artifacts and the effects of thermal emission that occurs at longer wavelengths. Therefore, the median value over this entire range of wavelengths is less sensitive to noise in the data than the value at a given wavelength. This operation minimizes the effects of albedo and possible remaining illumination variations. Because

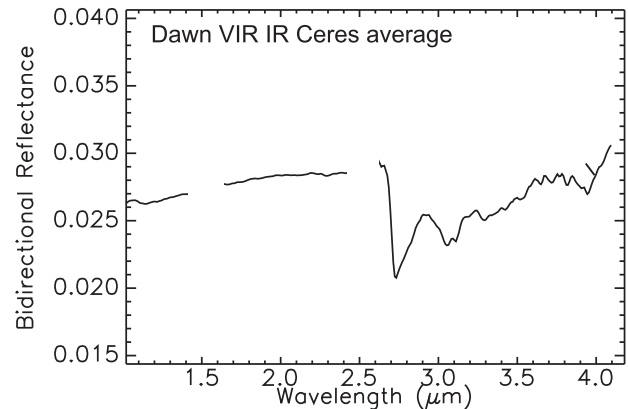


Fig. 1. Ceres average IR spectrum measured by Dawn's VIR IR imaging spectrometer ([De Sanctis et al., 2015](#)).

the surface composition of Ceres is very homogenous, with the exception of small, young areas that are spectrally different, it is assumed that, over time, any local component is progressively mixed with remote materials that have an average composition (impact gardening is one process). As a way to minimize the effects of mixture of local components (here, H₂O-rich materials) with the average surface composition, we divide each scaled VIR spectrum by the average scaled spectrum of Ceres ([Fig. 1](#)). After this operation, the absorption bands of the local component dominate in the spectra. The division is also an approximation of the effects of intimate mixing that occurs when multiple scattering dominates. This technique is commonly used for the search of absorption bands in spectral analysis of planetary surfaces.

We focused on the search of H₂O ice because this is the only component that has been linked to the identification of H₂O absorption bands in the VIR spectra of Ceres in the Oxo crater ([Combe et al., 2016](#)). For an automatic search of H₂O absorption bands, we compared spectra of H₂O-rich materials with ratioed VIR spectra. We used the technique of spectral shape fitting using the Multiple-Endmember Linear Spectral Unmixing Model (MELSUM: [Combe et al., 2008](#)). Each VIR spectrum in the ranges 1.1–1.4 μm and 1.6–2.4 μm was modeled by one ratioed VIR spectrum of the Oxo crater's H₂O-rich area used as a spectral endmember, plus a computed straight line (with variable slope and intercept for each pixel) to account for low-albedo, spectrally neutral materials and possible effects of Ceres' surface photometry that may affect the spectral slope. The analysis of each VIR spectrum is independent. The result is a weighing factor (mixing coefficient) associated to the H₂O-rich spectral endmember, and an estimate of the quality of fit by the Root-Mean Square (RMS). Finally, the H₂O-ice weighing factor divided by the RMS constitutes a very sensitive spectral criterion for the detection of H₂O ice. Above a certain threshold, we noted a sudden increase of the number of VIR spectra selected: this was an indication that the threshold was a limit between two different classes of spectra. As an independent way to assess

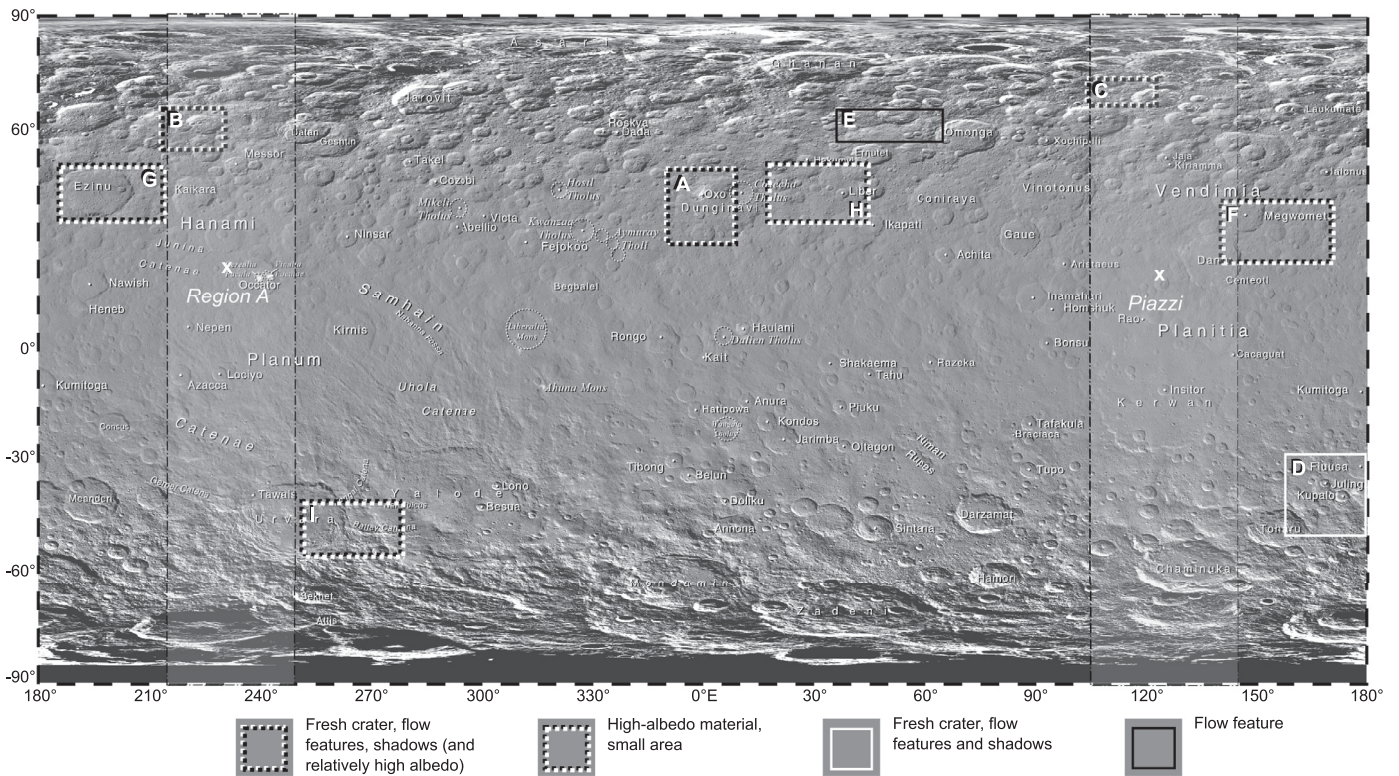


Fig. 2. Location of exposed H₂O-rich areas on Ceres. The rectangles indicate the boundaries of FC context images displayed in the next figures, and the line style refers to the type of surface feature that is observed. The grey vertical bands and locations marked by an X labeled Region A and Piazzia refer to the two areas identified as possible sources of H₂O vapor outgassing by Küppers et al. (2014). Projection: Simple Cylindrical; central meridian: 0 (adapted from Roatsch et al., 2016).

whether the VIR spectra selected automatically were compatible with H₂O absorption bands or not (false positive), we used visual inspection. We found that the threshold value was an adequate compromise between high sensitivity to the presence of H₂O absorption bands and few occurrences of false positive detections. Finally, the elimination of remaining false positives was done by visual inspection of all VIR spectra above that threshold. In Figs. 6–9, the threshold is defined by the value of 1265 in the color ramp.

3. Inventory and surface properties of exposed H₂O-rich areas on Ceres

Nine locations on Ceres were identified as H₂O-rich materials exposed at the surface (Fig. 2). Fig. 3 shows a selection of I/F spectra from single VIR pixels (no averaging) in order to illustrate the amplitude of measurement uncertainties (error bars) compared to the depth of H₂O absorption bands. Error bars are calculated from variations of the dark current, independently for each VIR detector element. For each VIR file, the dark current is measured at least twice: once at the beginning, once at the end, and sometimes in between. Removal of the dark current (*dark* in the equation below) is based on a linear interpolation between the dark current measurements that precede and that follow the acquisition of a targeted signal (a spectrum from the surface in Digital Numbers or DNs). For each wavelength, the uncertainty is calculated as follows: $Error = [\max(dark) - \min(dark)] / [DN - interpolated\ dark]$. This method implies that measured variations of the dark current are representative of the maximum and minimum values of the dark current that actually occurs during the acquisition of a file. It is necessary to make this assumption, because the dark current is not measured before and after each line of a given file. In Fig. 3, each error bar defines the envelope between $(1 + Error) \times Spectrum$ and $(1 - Error) \times Spectrum$. In the case of multiple observations of

the same site, the selection of spectra in Fig. 3 focuses on the earliest detections of H₂O that were acquired during Survey and HAMO, for which the spatial resolution is the lowest and therefore where the H₂O absorption bands are the weakest. In all cases, the absorption band at 2 μm is detected without ambiguity: its amplitude is greater than the measurement uncertainties, and it is visible over a range of wavelengths that corresponds to more than ten wavelength channels.

All H₂O detections are illustrated in Fig. 4 as average bidirectional spectra. Error bars are not shown for clarity. Note that Table 2 summarizes the characteristics of each site. All areas are located at latitudes above 30°, seven in the northern hemisphere and two in the southern hemisphere. Oxo Crater was the most observed (10 times by VIR) because it was a priority target. Four sites have been observed multiple times by VIR under illumination conditions that were favorable enough to provide spectra with detectable H₂O absorption bands. Fig. 5 shows the same spectra divided by the average spectrum of Ceres and scaled to the average reflectance level between 1.1 and 2.4 μm. All the spectra exhibit absorption bands at 2.0 μm, and most of them also have absorption features at 1.65 and 1.28 μm. The absorption band at 1.28 μm is the weakest of all, and thus it is not always detected when the signal-to-noise ratio is not high enough (Figs. 4 and 5, for example sites A and H). In five cases, a local maximum is visible at 3.1 μm, which is characteristic of the Fresnel peak of crystalline H₂O ice. Most of the spectra have a negative spectral slope that is also consistent with H₂O ice as a spectrally dominant component, however this is not systematic because in several cases, the H₂O-rich area is not spatially resolved by VIR, and therefore the areal mixture may not preserve the spectral slope of pure H₂O.

To better describe the surface and identify other possible features potentially related to H₂O, each site was also analyzed using FC clear images. As summarized in Table 2, all of the areas that

Table 2
Summary of all detections of exposed H₂O at the surface of Ceres by VIR.

Label in Fig. 4 and Fig. 5	Latitude °N	Longitude °E	Feature name	High albedo under sunlight	Morphological flow feature	Adjacent to shadowed, high-albedo areas	Spatially resolved with VIR	Area estimate from FC (m ²)	Area estimate from VIR (m ²)	Number of H ₂ O detections by VIR	VIR file names of H ₂ O detections
A	41.42	0.76	Oxo Crater	Yes	Yes	Yes	Yes		6.8 × 10 ⁶	9	483,757,616 483,760,468 483,786,868 486,828,195 486,829,447 487,089,319 506,266,095 509,827,248 515,317,211 517,049,003
B	69.66	114.81		Yes	Yes	Yes	Yes		< 3.3 × 10 ⁶ (1 Survey pixel)	3	483,770,816 487,075,414 487,346,608
C	61.32	221.06	Messor Crater	Yes	Yes	Yes	Yes		1.4 × 10 ⁶	5	486,803,364 487,065,770 497,917,630 511,834,141 513,761,900
D	−34.83	168.99	Juling Crater		Yes	Yes	Yes		Measured: 3.2 × 10 ⁶ Extrapolated: 6 × 10 ⁶	6	515,301,741 517,033,533 529,971,002 530,038,462 530,855,493 530,856,290
E	61.57	51.82			Yes		Yes (flow)		< 1.0 × 10 ⁴ (1 LAMO pixel)	1	510,672,534
F	29.60	155.07		Yes				1.0 × 10 ⁴ ± 6 × 10 ³	< 1.2 × 10 ⁶ (1 HAMO pixel)	1	494,522,179
G	42.20	199.51	Ezinu Crater	Yes				1.5 × 10 ⁴ ± 3 × 10 ³	< 1.0 × 10 ⁴ (1 LAMO pixel)	1	511,933,576
H	44.61	32.50		Yes				5 × 10 ³ ± 2 × 10 ²	< 1.0 × 10 ⁴ (1 LAMO pixel)	1	512,504,307
I	−47.92	265.46	Baltay Catena	Yes				2.8 × 10 ⁴ ± 6 × 10 ³	< 1.2 × 10 ⁶ (1 HAMO pixel)	1	496,635,057
VIR file name	Number of VIR spectra showing H ₂ O absorptions	Start Time	Dawn at Ceres mission phase	Target Center Distance (km)	Sub-solar latitude (°)	Incidence Angle (°)	Emergence Angle (°)	Pixel Scale (m)	Label in Fig. 4 and Fig. 5		
483,757,616	2	2015-05-01T13:05:50	RC3'	14,067.0	3.871	61	46	3462	A		
483,760,468	8	2015-05-01T13:53:22	"	14,067.8	3.872	54	44	3456			
483,786,868	3	2015-05-01T21:13:22	"	14,075.2	3.873	43	19	1100			
486,828,195	11	2015-06-06T02:02:09	Survey	4859.7	3.976	37	10	1099			
486,829,447	26	2015-06-06T02:23:01	"	4859.8	3.976	53	1	1101			
487,089,319	24	2015-06-09T02:34:13	"	4858.2	3.983	57	3	94			
506,266,095	101	2016-01-17T01:27:06	LAMO	840.4	3.383	44	14	96			
509,827,248	236	2016-02-27T06:39:39	"	841.9	3.064	62	32	99			
515,317,211	107	2016-04-30T19:39:02	"	844.1	2.464	53	22	102			
517,049,003	128	2016-05-20T20:42:14	"	854.6	2.251	69	16	1103			
483,770,816	3	2015-05-01T16:45:50	RC3	14,070.8	3.872	31	69	3463	B		
487,075,414	2	2015-06-08T22:42:28	Survey	4856.5	3.982	69	4	1102			
487,346,608	1	2015-06-12T02:02:22	"	4856.6	3.988	55	16	95			
486,803,364	1	2015-06-05T19:08:18	Survey	4856.7	3.976	65	18	1107	C		
487,065,770	2	2015-06-08T20:01:44	"	4855.7	3.982	60	49	388			
497,917,630	2	2015-10-12T10:26:02	HAMO	1936.9	3.89	70	12	100			
511,834,141	43	2016-03-21T12:07:52	LAMO	850	2.859	69	17	101			
513,761,900	17	2016-04-12T19:37:11	"	849.8	2.646	31	69	3463			
515,301,741	76	2016-04-30T15:21:12	LAMO	838.6	2.466	52	17	100	D		
517,033,533	5	2016-05-20T16:24:24	"	859.8	2.253	68	3	99			
529,971,002	18	2016-10-17T10:08:53	CXJ	1963.5	0.375	54	15	377			
530,038,462	34	2016-10-18T04:53:13	"	1963.8	0.364	44	30	390			
530,855,493	46	2016-10-27T15:50:23	"	1963.6	0.233	43	34	390			
530,856,290	5	2016-10-27T16:03:40	"	1962.8	0.233	41	38	392			
510,672,534	1	2016-03-08T01:27:45	LAMO	851.3	2.979	43	21	376	E		
494,522,179	1	2015-09-03T03:15:11	HAMO	1940.4	3.992	55	8	97	F		
511,933,576	5	2016-03-22T15:45:07	LAMO	846.9	2.848	54	10	94	G		
512,504,307	3	2016-03-29T06:17:18	LAMO	840.1	2.787	75	49	389	H		
496,635,057	1	2015-09-27T14:09:49	HAMO	1936.9	3.936	80	39	3427	I		

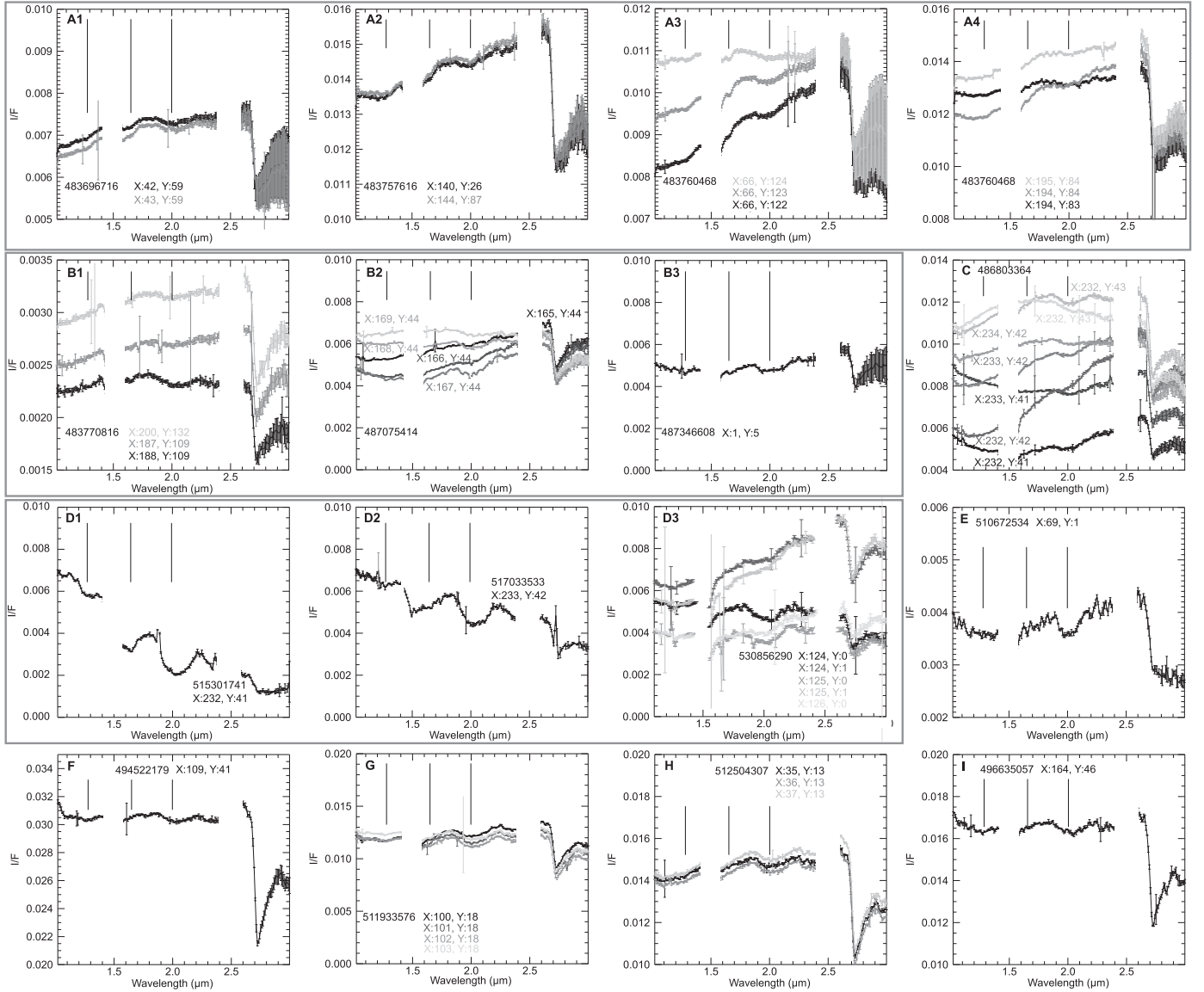


Fig. 3. Selection of VIR IR spectra of all H₂O-rich areas identified on Ceres. Vertical black lines indicate expected locations of H₂O absorption bands at 1.28, 1.65 and 2.0 μm. Each spectrum corresponds to a single VIR pixel. Error bars represent uncertainties related to variations of the dark current for each observation (see text for details). A1-A4 – (41.42°N, 0.76°E) Oxo Crater. B1-B3 – (69.66°N, 114.81°E). C – (61.32°N, 221.06°E). D1-D3 – (–34.83°N, 168.99°E) Juling Crater. E – (61.57°N, 51.82°E) Flow feature (Schmidt et al., 2017). F – (29.60°N, 155.07°E). G – (–47.92°N, 265.46°E) Baltnay Catena. H – (42.20°N, 199.51°E). I – (44.61°N, 32.50°E).

have H₂O-rich materials exposed at the surface present at least one visible characteristic, such as an albedo higher than the surrounding terrains, a morphology that indicates flow of material, or an adjacent shadow that may be persistent. From these observations, we found that several sites present similar characteristics. A more detailed description of our findings is available in the next four Sections: (3.1) On three occurrences (all in the northern hemisphere, including the Oxo crater), H₂O-rich materials with albedo slightly higher than surrounding terrains are associated with fresh impact craters presenting flow features or persistent shadows. (3.2) The Juling crater is a unique case because the H₂O-rich materials detected by VIR are present on a cliff with a steep pole-facing slope that was not under direct solar illumination at the time of the observations, but was made visible by secondary scattered illumination coming from the opposite crater wall, covered with high-albedo materials. (3.3) Another unique case is a flow feature that is not associated with high albedo materials nor persistent shadows at 61.57°N, 51.82°E. (3.4) Small areas, not spatially resolved by VIR,

with high albedo observed by FC, are found in four occurrences, including one in the southern hemisphere (Baltnay Catena).

3.1. Fresh crater, flow features, shadows and relatively high-albedo

Figs. 6–8 illustrate three H₂O-rich locations detected by VIR that have similar characteristics. These sites are located at latitudes higher than 42°, all in the northern hemisphere. They are all associated with fresh impact craters, as shown by the sharp rim crests and the boulders just outside the rim. They all contain material with higher albedo than the surrounding terrain whose location corresponds to the detection of H₂O absorption bands by VIR. In addition, these high-albedo surfaces correspond to crater wall material, near lobate flows, suggesting that they are affected by mass wasting or slope movements. In all three cases, the illuminated, H₂O-rich and high-albedo surface is on a pole-facing slope and adjacent to shadowed high-albedo areas, as revealed by FC images displayed in logarithmic scale. The upper parts of the

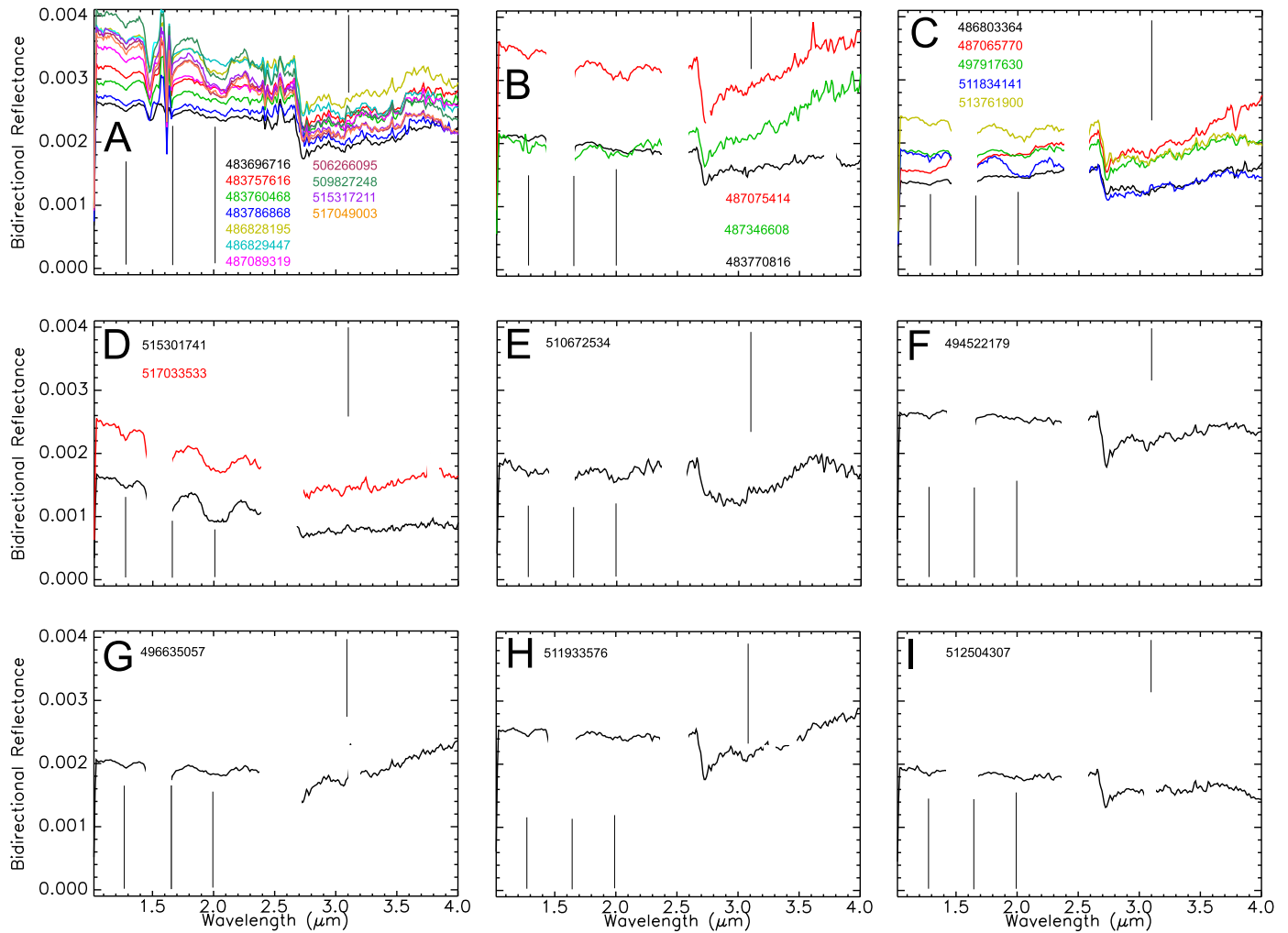


Fig. 4. Average bidirectional reflectance VIR IR spectra of all H₂O-rich areas identified on Ceres. Vertical gray lines indicate expected locations of H₂O absorption bands at 1.28, 1.65 and 2.0 μm, as well as the position of the Fresnel peak of crystalline H₂O ice 3.1 μm. The number of pixels per average spectrum is documented in Table 2. A – (41.42°N, 0.76°E) Oxo Crater. B – (69.66°N, 114.81°E). C – (61.32°N, 221.06°E). D – (–34.83°N, 168.99°E) Juling Crater. E – (61.57°N, 51.82°E) Flow feature (Schmidt et al., 2017). F – (29.60°N, 155.07°E). G – (–47.92°N, 265.46°E) Baltnay Catena. H – (42.20°N, 199.51°E). I – (44.61°N, 32.50°E).

wall, which have also high albedo, do not contain measurable H₂O absorption bands.

H₂O was previously detected in the 9.2-km diameter Oxo Crater (Combe et al., 2016). Since the first detection of H₂O in Oxo Crater made with Survey data, VIR made several subsequent targeted observations from LAMO, which are illustrated in color in Fig. 6. The improvement in spatial resolution (~100 m/pixel, which is about 10 times higher than images acquired in Survey) allows several, isolated H₂O-rich zones to be detected, and the total area of the H₂O-rich materials (6.8×10^6 m²) to be evaluated more accurately. In this data, H₂O is now clearly associated with surface materials with slightly higher albedo than adjacent terrains.

The second location is a 5.5-km diameter crater at 69.66°N, 114.81°E, where persistent shadows are combined with high-albedo materials (Platz et al., 2016; Ermakov et al., 2017) (Fig. 7). This crater was observed by VIR three times, exclusively from Survey orbit, and the H₂O absorption bands are present in only one or two VIR pixels each time. Each of these few VIR pixels cover most of the crater, as well as surrounding areas. Because of the similarity with the other two craters, we make the hypothesis that H₂O-rich materials have often relatively higher albedo than its surrounding terrains, and are adjacent to shadowed areas in the crater floor.

In this study, we identified a third crater (Fig. 8) at 61.32°N, 221.06°E that is 6.1 km in diameter, where H₂O has been detected

by VIR from Survey, HAMO and LAMO orbits. Only VIR LAMO pixels are illustrated in color in Fig. 8.

3.2. Fresh crater, flow features and shadows

Juling Crater (Fig. 9) is only one of the two sites in the southern hemisphere where exposed H₂O-rich materials were found (De Sanctis et al., 2016). The H₂O-rich materials are found in two VIR LAMO observations, and are all located near the top of northern wall. This is the place with the second most intense H₂O absorption bands on Ceres after LAMO observations of Oxo. In the FC image, most of the crater wall's surface is in the shadow, and it is only visible because of scattered light from adjacent terrains and the opposite wall, which is covered by high-albedo materials.

According to FC observations, the northern, pole-facing wall has steep slopes and a sharp scarp. At the base of the wall, a smooth material with steep margins, longitudinal grooves and lobate in planar view extends toward the crater center, which is consistent with some sort of material flow. H₂O-rich materials correspond to the sharp scarp and therefore may have their source directly on the wall, where mass wasting exposes fresh material. This suggests that H₂O is present in the subsurface in the immediate vicinity of the crater, at least on the northern side. Alternatively, the H₂O-rich area has topography that looks like it would shadow

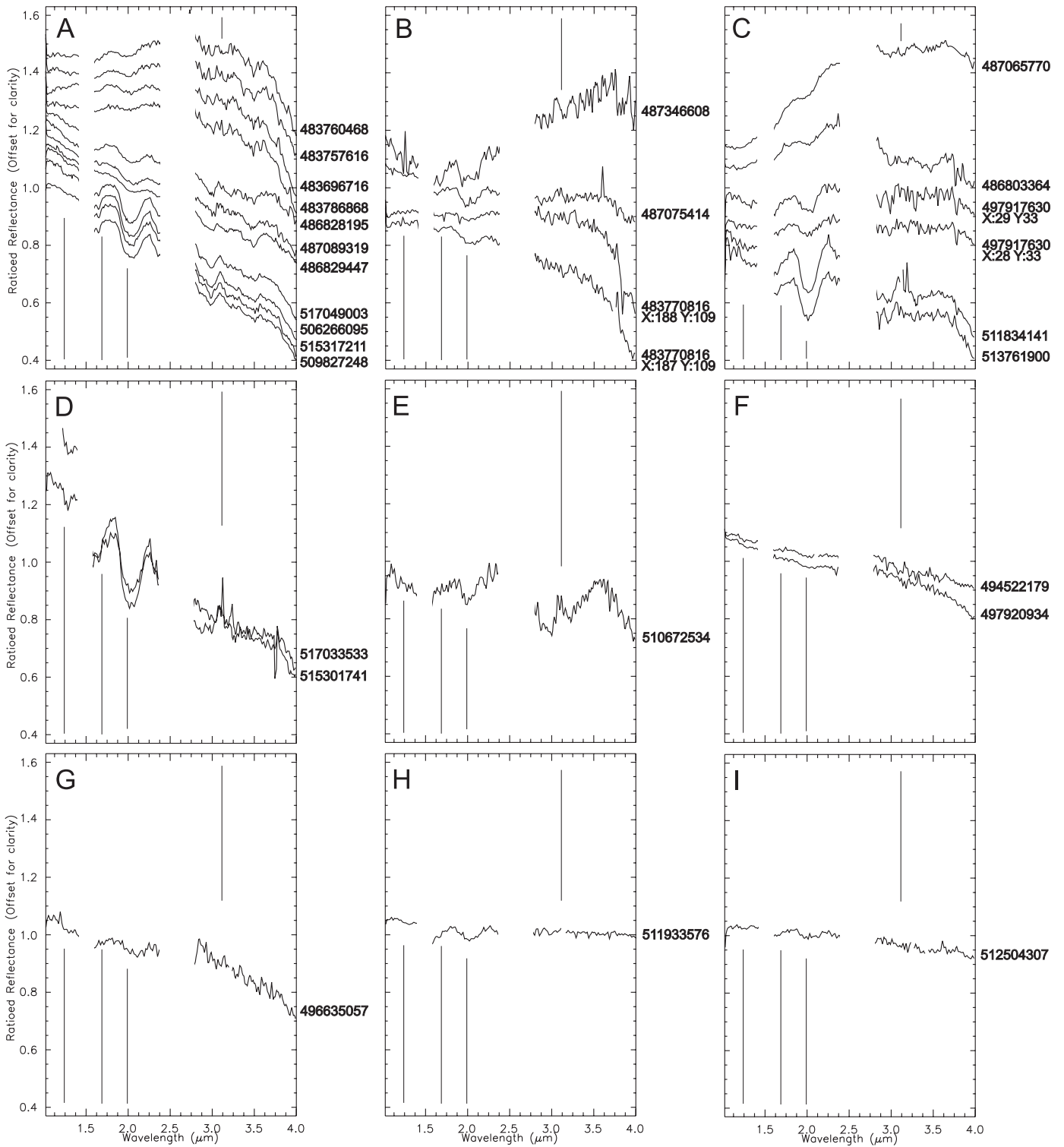


Fig. 5. Average ratioed and scaled reflectance VIR IR spectra of all H₂O-rich areas identified on Ceres. Vertical gray lines indicate expected locations of H₂O absorption bands at 1.28, 1.65 and 2.0 μm, as well as the position of the Fresnel peak of crystalline H₂O ice 3.1 μm. A – (41.42°N, 0.76°E) Oxo Crater. B – (69.66°N, 114.81°E). C – (61.32°N, 221.06°E). D – (–34.83°N, 168.99°E) Juling Crater. E – (61.57°N, 51.82°E) Flow feature (Schmidt et al., 2017). F – (29.60°N, 155.07°E). G – (–47.92°N, 265.46°E) Baltnay Catena. H – (42.20°N, 199.51°E). I – (44.61°N, 32.50°E).

the pole-facing wall regardless of the time of day; therefore, if it is shadowed a large fraction of the time, it might be a potential site for cold trapping of water molecules.

The upper part of the illuminated opposite wall and rim have high albedo but they do not contain H₂O, according to VIR spectra.

3.3. Flow feature with moderate albedo

Fig. 10 shows an 8-km long flow feature, identified among other ones by Schmidt et al. (2017), which is not associated with a fresh impact crater and does not present high-albedo materials.

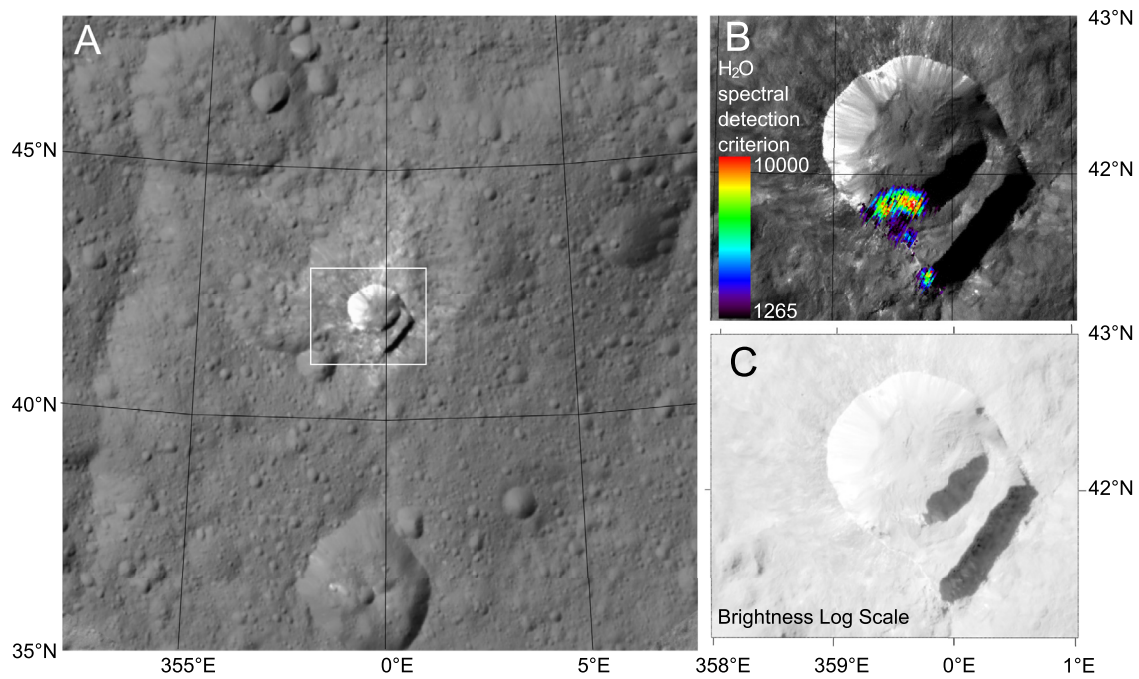


Fig. 6. FC imagery context of the H₂O-rich material area at 41.42°N, 0.76°E associated to Oxo Crater and southeastern scarp. A – Mosaic from HAMO observations displayed in Lambert conformal conic projection. The white rectangle delimits the close-up view on the right. B – Close-up view of Oxo crater from image FC21A0052044_16017012741F1F acquired from LAMO. Colored pixels represent VIR H₂O detections of H₂O from LAMO. Values are mixing coefficients divided by the RMS (i.e., the quantity that was used to identify H₂O from VIR spectra). C – Same FC image as B, with brightness display stretched in logarithmic scale in order to visualize both illuminated and shadowed areas.

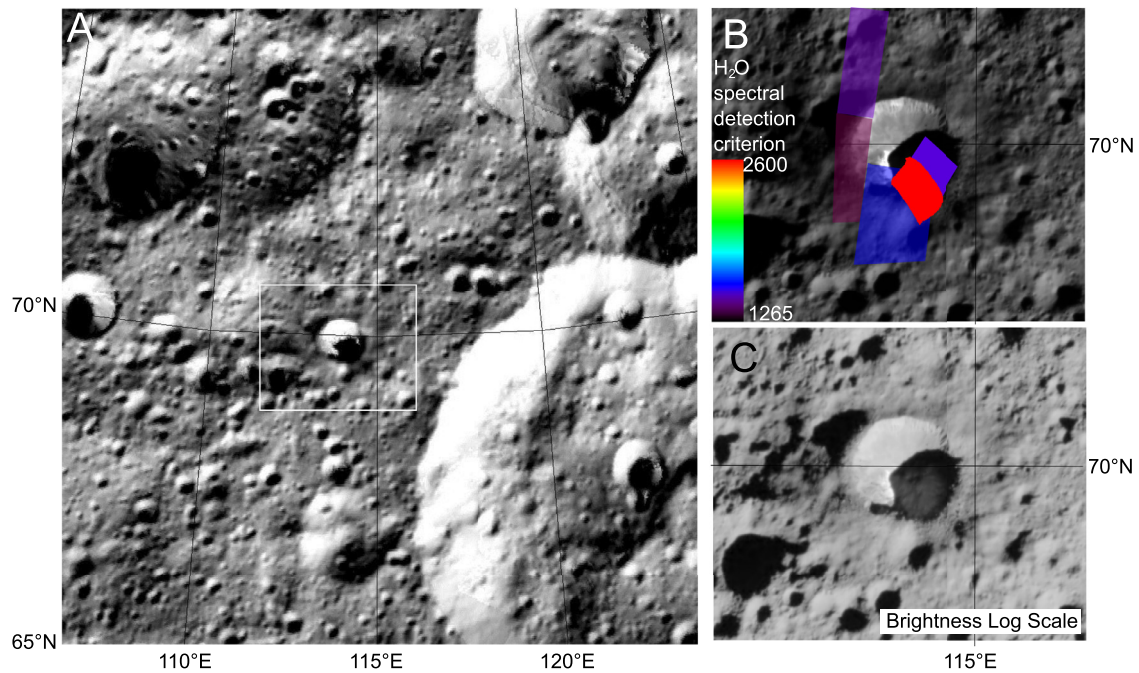


Fig. 7. FC imagery context of the H₂O-rich material area at 69.66°N, 114.81°E inside a fresh impact crater (Platz et al., 2016). A – Mosaic from HAMO observations displayed in Lambert conformal conic projection. The white rectangle delimits the close-up view on the right. B – Close-up view of the fresh crater from image FC21A0046607_15351072425F1D acquired from LAMO. Colored pixels represent VIR H₂O detections of H₂O from LAMO. Values are mixing coefficients divided by the RMS (i.e., the quantity that was used to identify H₂O from VIR spectra). C – Same FC image as B, with brightness display stretched in logarithmic scale in order to visualize both illuminated and shadowed areas.

H₂O is detected on a small area (a single VIR pixel from LAMO) in the middle of this flow feature, adjacent to a shadowed area. The spectrum (Figs. 4E and 5E) exhibits an absorption band at 2.0 μm and a peak at 3.1 μm, which is consistent with the Fresnel peak in crystalline H₂O ice. Analysis of brightness variations within the shadowed areas does not indicate the presence of high-albedo

materials. This flow feature is one case among others that initiates from an old and degraded crater rim and progresses downward towards the floor. Both the front and side boundaries of the flow are steep; a longitudinal ridge delimits the sides. According to Schmidt et al. (2017), these types of features occur at high latitudes (predominantly above 50°) and are characteristic of

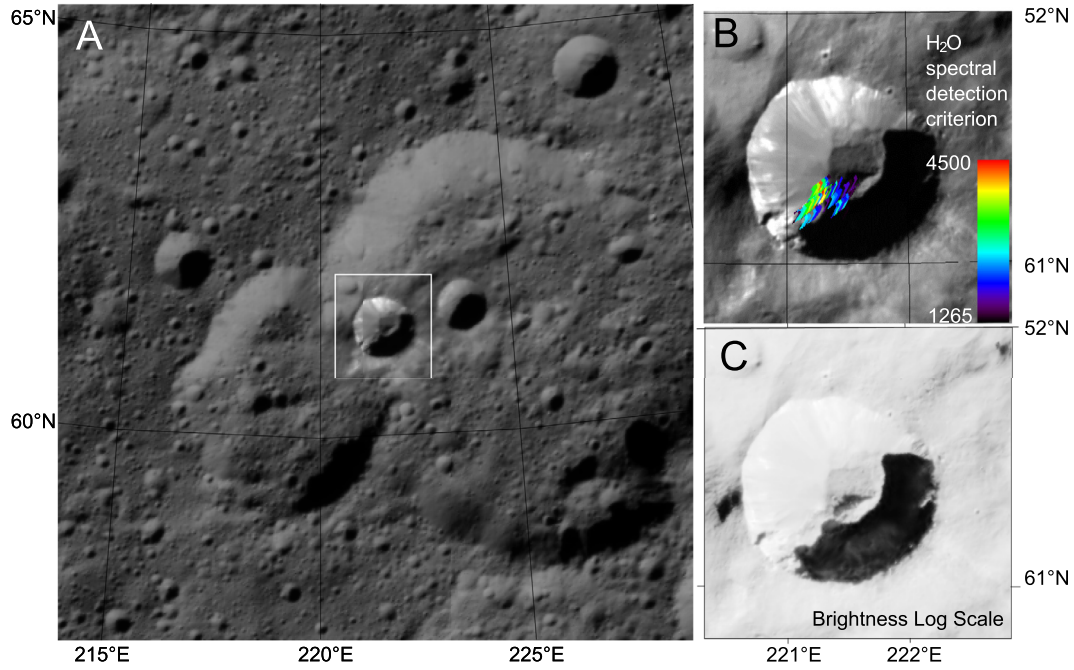


Fig. 8. FC imagery context of the H₂O-rich material area at 61.32°N, 221.06°E inside a fresh impact crater included in Messor Crater (Combe et al., 2018). A – Mosaic from HAMO observations displayed in Lambert conformal conic projection. The white rectangle delimits the close-up view on the right. B – Close-up view of the fresh crater from image FC21A0047863_15358091114F1G acquired from LAMO. Colored pixels represent VIR H₂O detections of H₂O from LAMO. Values are mixing coefficient divided by the RMS (i.e., the quantity that was used to identify H₂O from VIR spectra). C – Same FC image as B, with brightness display stretched in logarithmic scale in order to visualize both illuminated and shadowed areas.

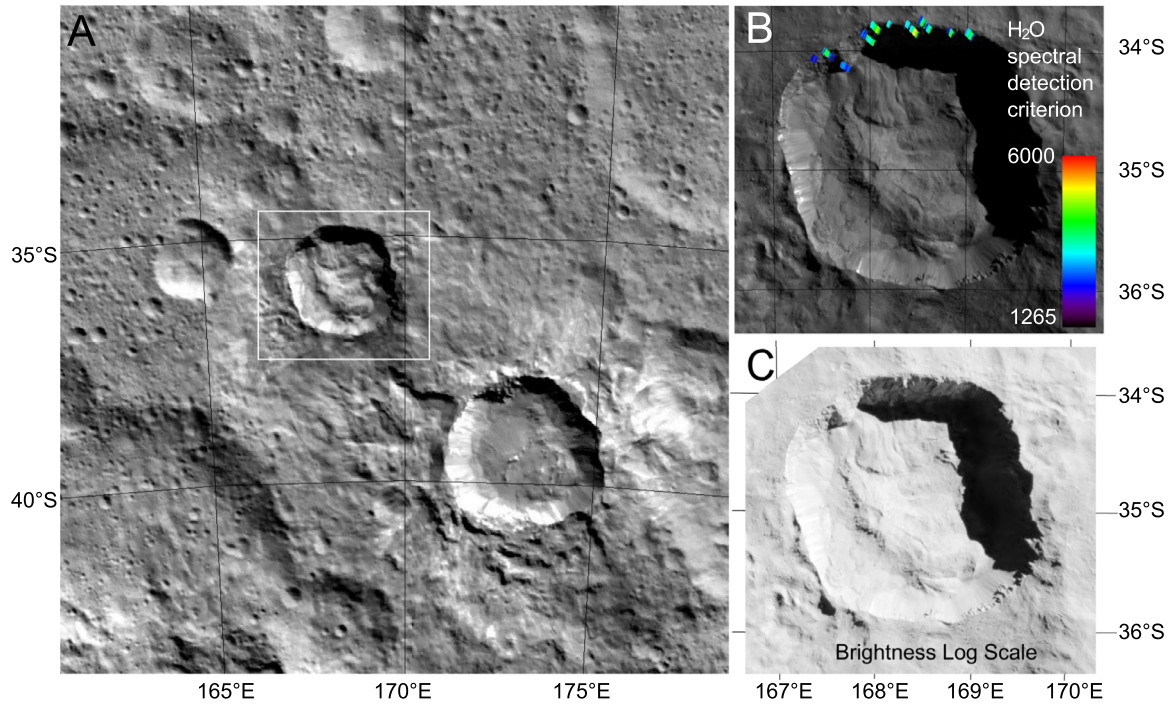


Fig. 9. FC imagery context of the H₂O-rich material area at 34.83°S, 168.99°E on the northern cliff of the Juling crater. A – Mosaic from HAMO observations displayed in Lambert conformal conic projection. The white rectangle delimits the close-up view on the right. B – Close-up view of the Oxo crater from image FC21A0052009 acquired from LAMO. Colored pixels represent VIR H₂O detections of H₂O from LAMO. Values are mixing coefficients divided by the RMS (i.e., the quantity that was used to identify H₂O from VIR spectra). C – Same FC image as B, with color display stretched in order to enhance the contrast within the shadowed area.

ice-cemented materials. Several impact craters are present on the flow itself, which suggest a flow feature that is old compared to the ones described in Section 3.1 and 3.2. Since H₂O is detected only on a small area of the flow, this suggests that H₂O is present in the bulk of the flow, but is not generally exposed. This obser-

vation may imply that H₂O was probably at the surface during the evolution of Ceres, then sublimation obliterated all of it, making it spectrally undetectable. At present, the flow may be covered by a lag deposit that masks most of the ice, assuming the composition is a mixture of H₂O ice and mineral particles. This interpretation is

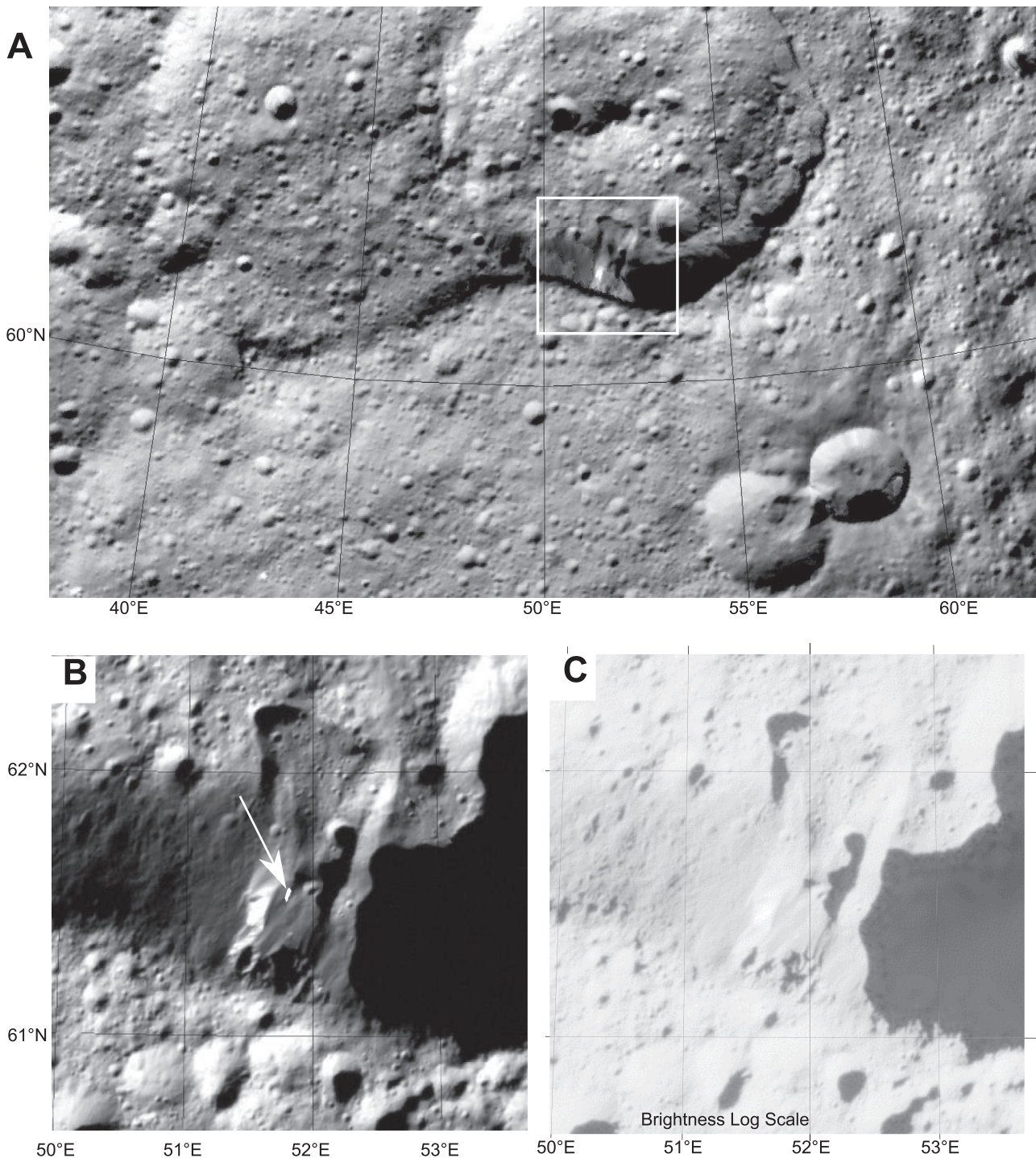


Fig. 10. FC imagery of the H₂O-rich material area at 61.31°N, 51.82°E displayed in Lambert conformal conic projection (Schmidt et al., 2017). A – Mosaic from HAMO observations. The white rectangle delimits the close-up view on the right. B – Close-up view of the flow-like feature that exhibits H₂O absorption bands in one VIR spectrum (in white, at the tip of the arrow) from observation 510,672,534, displayed in white, superimposed on a projected FC image (FC21A0048919_15363202934F1G). C – Same FC image as B, with color display stretched in order to enhance the contrast within the shadowed area.

supported by the fact that the surface of the large flow is cratered, except the small area where the detection occurs (upslope on the crater wall, where the surface is smooth and fresher). The local detection of H₂O by VIR may reveal an episodic exposure of H₂O ice, either from an impact (although no evidence is visible), or from mechanical disturbance of the surface due to movement of the flow, or from ice sublimation.

3.4. Small, high-albedo areas under direct sunlight

The last type of H₂O-rich areas that we identified is small (<0.1 km²) and of high-albedo area, whereas the morphology does not indicate a nearby flow feature, and the illumination conditions do not indicate persistent shadows. Four sites present similar traits, although only three of them seem to be associated with

Table 3Description of the framing camera HAMO and LAMO observations of the H₂O-rich material area at 42.20°N, 199.51°E.

Figure Number	Framing Camera file name	Time	Pixel Scale (m)	Solar Longitude (°)
Fig. 11B	FC21B0042226_15245075026F1E	2015-09-02T07:50:26	142	97.47
Fig. 11C	FC21B0052773_16021091525F1E	2016-01-21T09:15:25	34.86	123.59

Table 4Description of the framing camera LAMO observations of the H₂O-rich material area at 29.60°N, 155.08°E.

Figure Number	Framing Camera file name	Time	Pixel Scale (m)	Solar Longitude (°)
Fig. 12B	FC21B0041475_15237105237F1G	2015-08-25T10:52:37	137	95.99
Fig. 12C	FC21A0046904_15353034740F1G	2015-12-19T03:47:40	36.16	117.46

Table 5Description of the framing camera LAMO observations of the H₂O-rich material area at 47.92°S, 265.46°E, near Baltnay Catena.

Figure Number	Framing Camera file name	Time	Pixel Scale (m)	Solar Longitude (°)
Fig. 13B	FC21B0039530_15230123844F1G	2015-08-18T12:38:44	138	94.69
Fig. 13C	FC21B0049218_16001154324F1D	2016-01-01T15:43:24	34.32	119.95

Table 6Description of the framing camera LAMO observations of the H₂O-rich material area at 44.61°N, 32.50°E.

Figure number	Framing Camera file name	Time	Pixel Scale (m)	Solar Longitude (°)
Fig. 14B	FC21B0039801_15231214233F1G	2015-08-19T21:42:33	138	94.95
Fig. 14C	FC21B0046455_15350152140F1A	2015-12-16T15:21:40	36.77	117.00

the pole-facing slope of a small impact crater. Although VIR does not spatially resolve any of these areas, the detection of H₂O is systematically associated with small high-albedo areas that can be observed with the FC images. All these sites were identified in FC images acquired in HAMO, although none of them were spatially resolved. However, multiple LAMO FC images are available for all of them, where the albedo feature is always spatially resolved and is covered by several pixels. Fig. 11A presents the context FC imagery of the site at 42.20°N, 199.51°E within the Ezinu crater, Fig. 11B illustrates the first FC HAMO observation where the albedo feature is visible, and Fig. 11C shows the first LAMO image. Table 3 lists all images displayed in Fig. 11. A similar case was found at 29.60°N, 155.08°E, where FC images are shown in Fig. 12, and Table 4 provides image information. A third site at 47.92°S, 265.46°E near Baltnay Catena (Fig. 13) resembles the two aforementioned sites, except that it comprises three distinct spatially-resolved areas of high albedo, and possibly four secondary high-albedo areas that are not spatially resolved in FC images. Table 5 provides information for the FC images. The fourth site at 44.61°N, 32.50°E has also a small area of higher albedo (Fig. 14), however, unlike the previous three, it is difficult to identify an impact crater in the FC LAMO images (Table 6).

In all four cases, the high-albedo material was observed consecutively for about one terrestrial year (1/5th of one Ceres year). HAMO observations began for solar longitudes ~95°, shortly after summer solstice (where solar longitude Ls = 90°), and the last LAMO observations were acquired at Ls ~160°, which is before the autumn equinox.

4. Interpretation of the distribution and observed characteristics of exposed H₂O-rich areas

4.1. Spectral modeling

In a previous study, Combe et al. (2016) compared VIR spectra of the Oxo crater with laboratory spectra of mineral hydrates and H₂O ice, the latter providing the best fit. In all the cases, the shape of the 2.0 μm absorption band was the main spectral feature for

the determination of the composition in H₂O ice, this absorption band is symmetric and centered at 2.0 μm, which is not the case for any of the mineral hydrates under consideration. Additional measurements (Sandeep, personal communication) confirm that even mineral hydrates with higher solvation states (when a larger number of H₂O molecules are bonded to the mineral) than those initially used samples, and with sample temperatures more relevant to the surface of Ceres (180 K instead of 110 K), do not exhibit H₂O absorption bands similar to those measured by VIR in the Oxo crater. In the present study, Figs. 4 and 5 show that in all nine H₂O-rich areas, the most diagnostic absorption band is always centered at 2.0 μm and symmetric, which provides straightforward spectral evidence that the H₂O-rich component is exposed H₂O ice. Most VIR spectra correspond to pixels that cover more than the H₂O-rich areas, because most of the nine sites are not spatially resolved. In the measured spectra by VIR, the large pixel footprint results in a contribution by H₂O-ice and a contribution by the surface materials around the H₂O-rich area, linearly combined (areal mixture). Combe et al. (2016) also determined that the VIR spectra of Oxo could be modeled by linear combinations of the average spectrum of Ceres with H₂O-ice spectrum.

In the present study, the H₂O-rich area associated with Oxo is spatially resolved by VIR. As a consequence, VIR spectra centered on this area exhibit the strongest H₂O absorption bands measured by VIR (42% in Fig. 15). Spectra of the Juling crater have also very strong H₂O absorption bands, which are presented in Raponi et al. (2018).

VIR spectra of Oxo provided the opportunity to perform further modeling. Raponi et al. (2016) obtained adequate spectral modeling results based on the radiative transfer theory of intimate mixing, using H₂O ice and various phyllosilicates found on Ceres.

Fig. 15 illustrates a test performed with pure H₂O ice. We used MELSUM (Combe et al., 2008) with different settings from those used in section 2.4. Here, we selected laboratory spectra of H₂O-ice samples with different grain size distribution as spectral endmembers. The temperature of the H₂O-ice samples that provide the reference spectra is 110 K. We used a computed straight line to account for high incidence angle, or low-albedo, spectrally

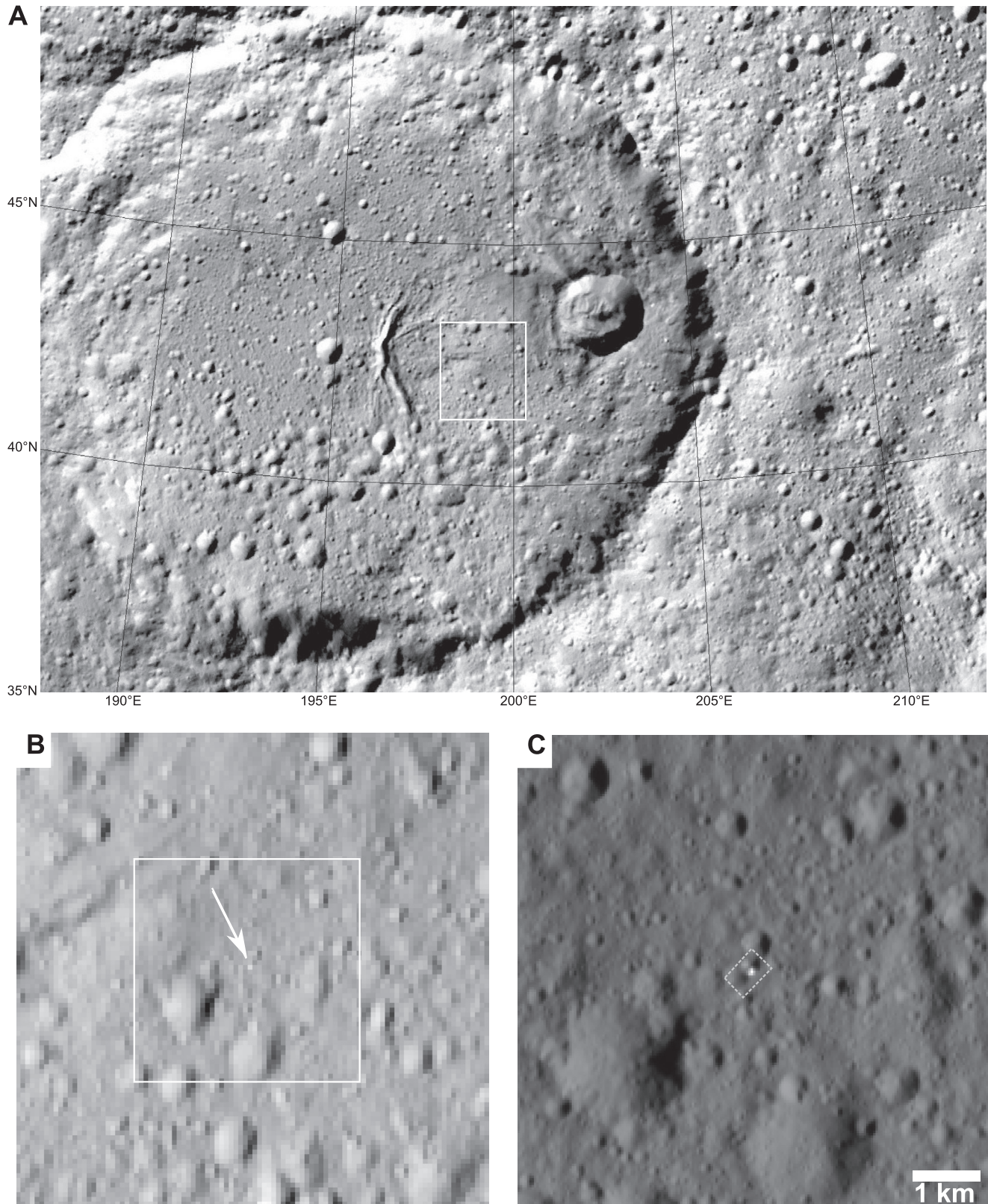


Fig. 11. FC imagery context of the H₂O-rich material area at 42.20°N, 199.51°E within the Ezinu crater (Combe et al., 2018). A – Mosaic displayed in Lambert conformal conic projection. The white rectangle delimits the close-up view on the right. B – Close-up view from the earliest observation of the high-albedo area (white arrow) with FC from HAMO: unprojected portion of FC21B0042226_15245075026F1E. C – Framing Camera LAMO unprojected portion of FC21B0052773_16021091525F1E of the H₂O-rich material area at 42.20°N, 199.51°E. The polygon indicates the footprint of the VIR pixels. Data information and scale are provided in Table 3.

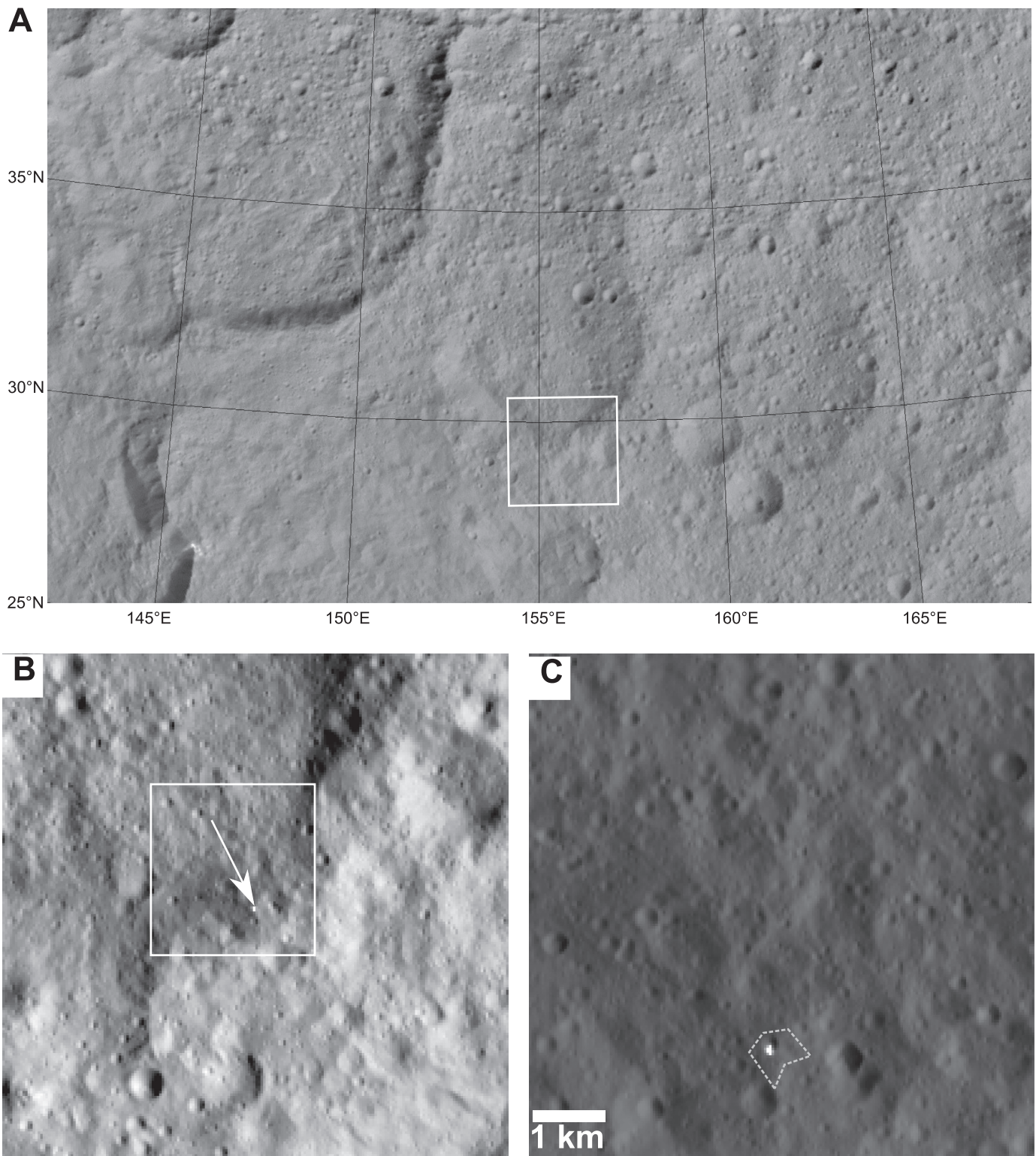


Fig. 12. FC imagery context of the H₂O-rich material area at 29.60°N, 155.08°E. A – Mosaic displayed in Lambert conformal conic projection. The white rectangle delimits the close-up view on the right. B – Close-up view from the earliest observation of the high-albedo area (white arrow) with FC from HAMO: unprojected portion of FC21B0041475_15237105237F1G. C – Framing Camera LAMO unprojected portion of FC21A0046904_15353034740F1G of the H₂O-rich material area at 29.60°N, 155.08°E. The polygon indicates the footprint of the VIR pixel. Data information and scale is provided in [Table 4](#).

neutral materials, and possible effects of Ceres' surface photometry that may affect the spectral slope. MELSUM automatically selected three reference spectra (combining three different grain sizes) to calculate the modeled spectrum that best fits the VIR spectrum. The result show that the shape of all H₂O-ice spectral

features, such as the absorption bands at 1.28, 1.65 and 2.0 μm, and the Fresnel peak at 3.1 μm are also modeled accurately by a linear combination of H₂O-ice spectra. Model residuals have some anomalies, the amplitude of which is of the same order than measurement uncertainties (error bars) between 3.0 and

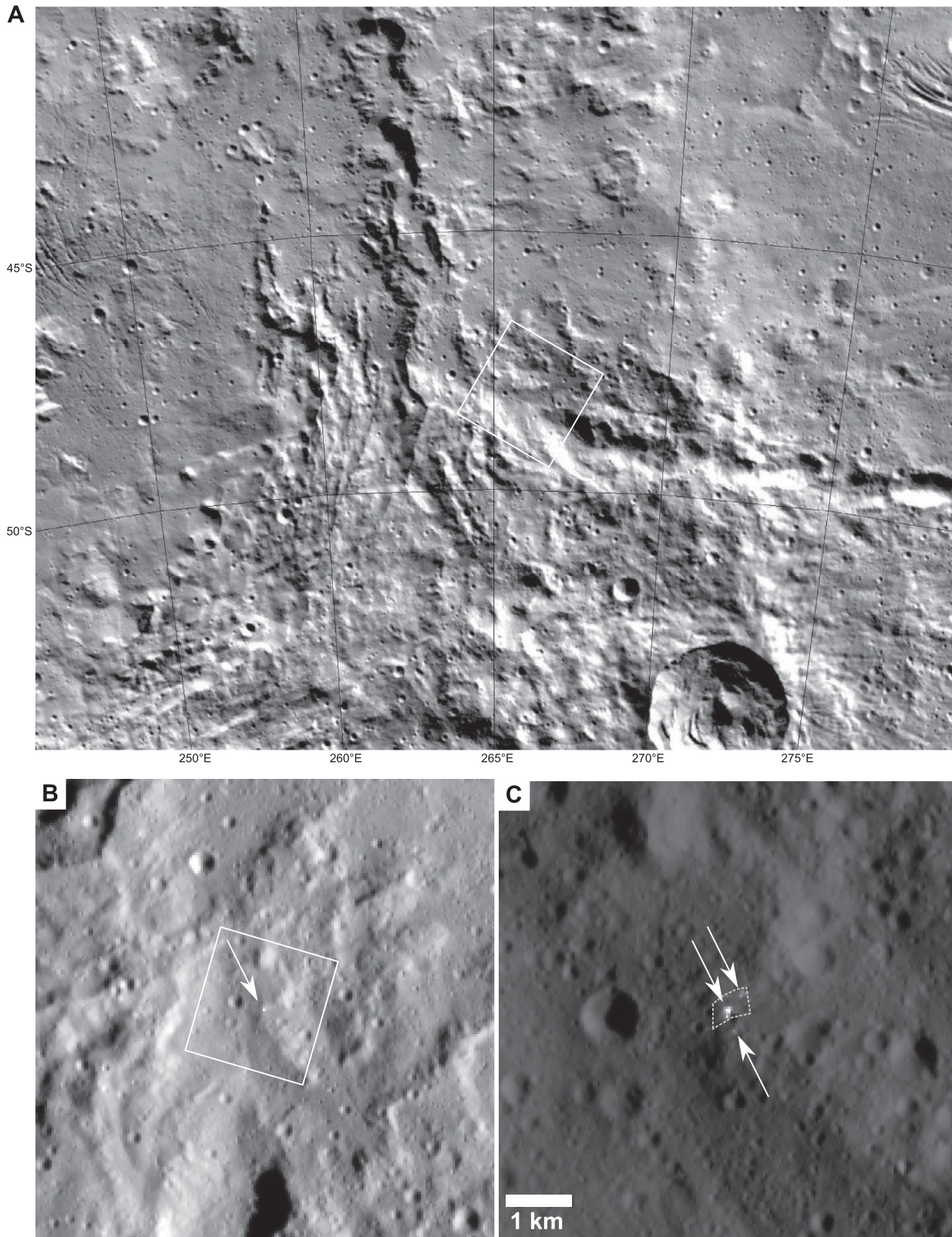


Fig. 13. FC imagery context of the H₂O-rich material area at 47.92°S, 265.46°E. A – Mosaic displayed in Lambert conformal conic projection. The white rectangle delimits the close-up view on the right. B – Close-up view from the earliest observation of the high-albedo area (white arrow) with FC from HAMO: unprojected portion of FC21B0039530_15230123844F1G. C – Framing Camera LAMO unprojected portion of FC21B0049218_16001154324F1D of the H₂O-rich material area at 47.92°S, 265.46°E, near Baltay Catena. The polygon indicates the footprint of the VIR pixel, and the arrows points at three distinct small, high-albedo features. Data information and scale is provided in Fig. 13.

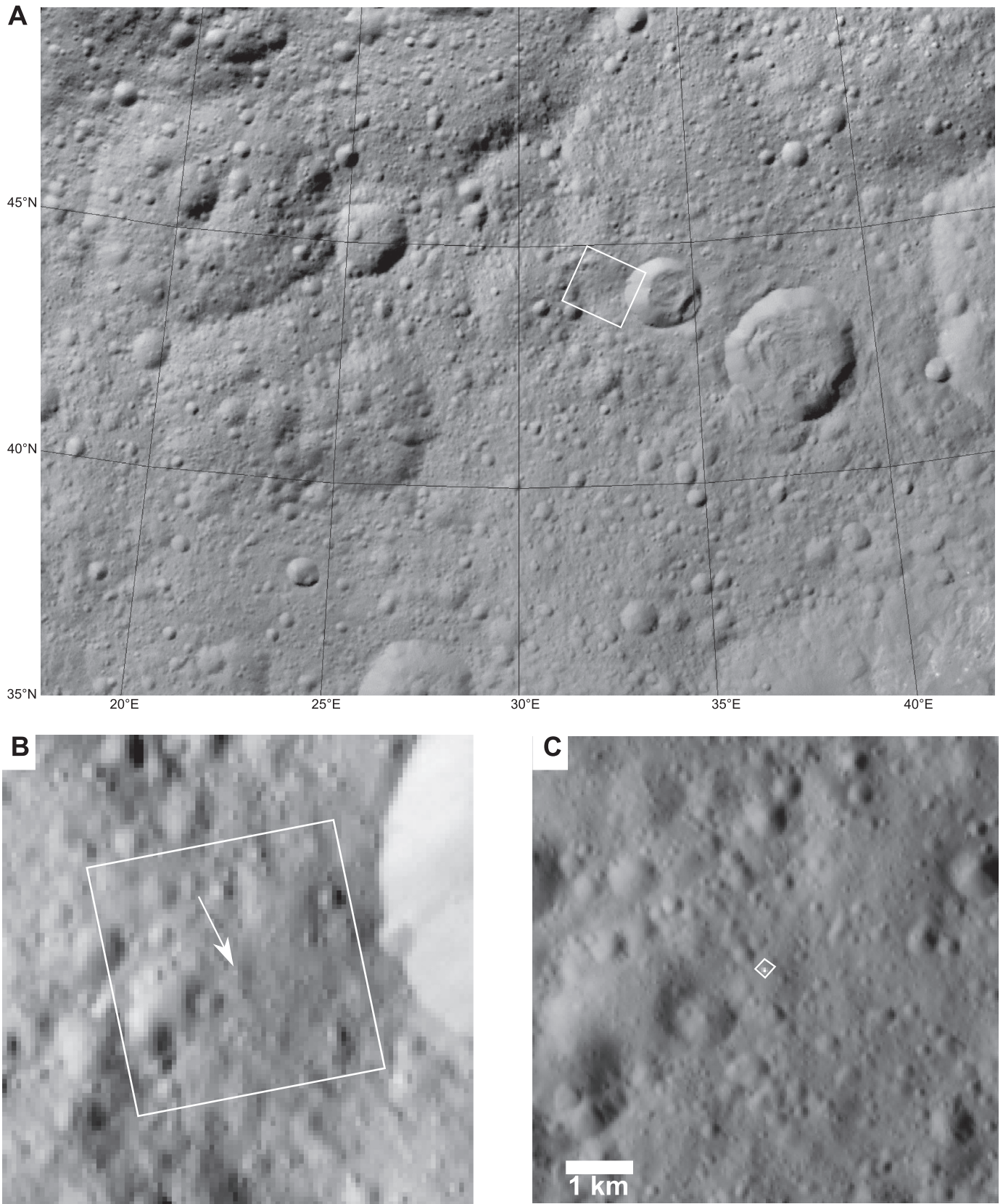


Fig. 14. FC imagery context of the H₂O-rich material area at 44.61°N, 32.50°E. A – Mosaic displayed in Lambert conformal conic projection. The white rectangle delimits the close-up view on the right. B – Close-up view from the earliest observation of the high-albedo area (white arrow) with FC from HAMO: unprojected portion of FC21B0039801_15231214233F1G. C – Framing Camera LAMO unprojected portion of FC21B0046455_15350152140F1A of the H₂O-rich material area at 44.61°N, 32.50°E. The polygon indicates the footprint of the VIR pixel. Data information and scale is provided in [Table 6](#).

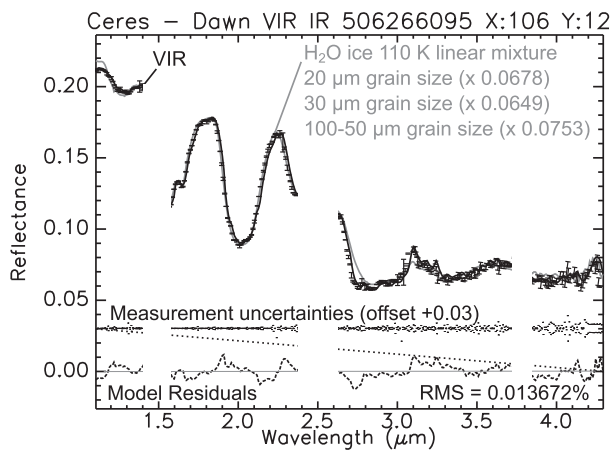


Fig. 15. VIR IR reflectance spectrum of Oxo acquired during LAMO modeled by a linear combination of three H₂O ice spectra (Hansen, 2009; Filacchione et al., 2016) with different grain size distributions and a low-albedo, spectrally neutral component (dotted line).

4.3 μm, and larger than measurement uncertainties between 1.1 and 3.0 μm. Uncertainties associated with the model are likely due in first order to the temperature in the simulated spectra of H₂O ice (110 K), which is lower than Ceres surface temperature by several tens of K. In particular, the shape of the H₂O absorption bands is sensitive to temperature variations (e.g. Hansen 2009). The limited distribution of grain sizes may also be a factor in the model, since the depth and width of an absorption band tend to increase with increasing grain size. In spite of the assumptions in the model and the observed anomalies in the residuals, the presence of spectral features associated with crystalline H₂O ice (the absorption bands and the Fresnel peak), both in the VIR spectrum and in the model have some significance. This modeling is supported by previous investigations which found that the H₂O-rich component on Ceres is crystalline H₂O ice (Combe et al., 2016; Raponi et al., 2018). Additional contributions by other surface components in VIR spectra may exist when the size of VIR pixels does not spatially resolve the H₂O-rich area. The H₂O ice may also be mixed with a spectral component similar to the average surface of Ceres, which is spectrally neutral in the range of wavelengths of the H₂O absorption bands. These results as well as those obtained by Raponi et al. (2016) indicate the non-uniqueness of the models, because similar quality of fit is obtained by selecting 20–100 μm grain sizes in linear combination of spectra, or by using larger grain sizes (100–200 μm) for H₂O ice and adding mineral components using the radiative transfer theory.

4.2. Distribution of H₂O-rich areas

There are two main characteristics that define the nine H₂O-rich areas detected by VIR: (1) The latitude is always above 30° (in both hemispheres); and (2) the area is limited to a few km² (6.8 at maximum in Oxo, which comprises three distinct areas), and most often on the order of 1 km². The maximum latitude of H₂O detection is only limited by the absence of coverage of the polar regions by VIR and by large incidence angles that create large areas of casted shadows where no observation is possible.

4.2.1. Comparison between VIR observations and other evidences of H₂O-rich materials

The latitude range is an indication of the role of illumination and surface temperature in the stability of the H₂O-rich component. The sublimation rate of H₂O ice, which varies by several orders of magnitude across all latitudes and throughout a

complete revolution of Ceres around the sun (Landis et al., 2017), may explain the trend observed in the distribution of exposed H₂O ice. The temperature of the surface, illuminated or shadowed, depends on latitude, as does the depth to the ice. The existence of H₂O ice above 30° latitude implies a recent exposure or a form of replenishment process, either endogenous (associated with areas of weak zones, or by mechanical exposure such as landslides or seismic shaking from nearby impacts), or surficial (such as the migration of H₂O molecules into cold traps), or external (such as meteorite impacts). This location is also where the sublimation rate, especially in poleward facing slopes, becomes very small.

In certain cases, such as the area at (44.61°N, 32.50°E in Fig. 14), the H₂O-rich material is exposed on surfaces that do not show any remarkable topographic features (not on a pole-facing slope, for example), and thus does not appear to be a cold trap. For that particular location, the aspect of the surface topography and morphology rules out the association with any impact, and thus with any form of external replenishment of H₂O. All the other small, high-albedo H₂O-rich areas are associated with small impact craters, however, the geological context and topography of these sites do not indicate any remarkable characteristics that could explain the existence of a cold trap. In absence of any other evidence, the most robust hypothesis is that a certain amount of H₂O ice present in the subsurface became exposed.

The four fresh impact craters (three in the northern hemisphere and Juling) that show flow features on the wall and floor likely favored the occurrences of landslides in an H₂O-rich terrain, which could expose that material. In the hypothesis that H₂O-ice is the main component, the sharp topography that casts shadows on their pole-facing slope likely slows down the sublimation rate, which in turns increases the probability of detection over periods of several months, as was done by Dawn's instruments.

The global distribution of H₂O-equivalent hydrogen from GRaND measurements (Fig. 16) shows minimum values along the equator and maximum values near the poles. All detections of exposed H₂O ice by VIR occur where the average regional abundance of H₂O-equivalent hydrogen is above 20 wt. %. The depth-to-ice on Ceres depends on latitude, as temperatures vary between the poles and the equator. In the polar regions, the regolith appears ice-free in images and reflectance spectra, although GRaND does detect H in abundance near the surface. These observations are consistent with models of ice retreat that suggest that the ice-free topmost layer may be less than a centimeter thick (Schorghofer, 2016). At the equator, the expected depth to the ice table depends on the physical properties of the lag (Fanale and Salvail 1989), but could be less than a meter (Prettyman et al., 2016). Such a thin overburden layer makes it plausible that ice can be exposed by minor mechanical disturbances, such as impacts and landslides.

The overlying ice-free layer has two functions for the preservation of subsurface ice. First, it represents a diffusive barrier that water molecules must traverse, and second, it attenuates the temperature amplitude, such that the peak temperatures felt by the buried ice are less than those on the very surface. This causes a significant difference between the sublimation rate of exposed ice (Landis et al., 2017) and that of buried ice. It explains why exposed ice is currently rare on Ceres, despite the claim of ubiquitous presence of H₂O ice in the subsurface (e.g., Prettyman et al., 2016; Castillo-Rogez et al., 2018, in press).

4.2.2. Comparison between Dawn/VIR and Herschel observations

H₂O at the surface of Ceres was inferred from the interpretation of H₂O outgassing that was revealed by spectra from the Herschel telescope Küppers et al. (2014). No detection of H₂O has been made by Dawn on the two sites identified as Piazzi and Region A in Herschel observations (Figs. 2 and 16). However, since other H₂O-rich objects in the Main Asteroid Belt are observed by

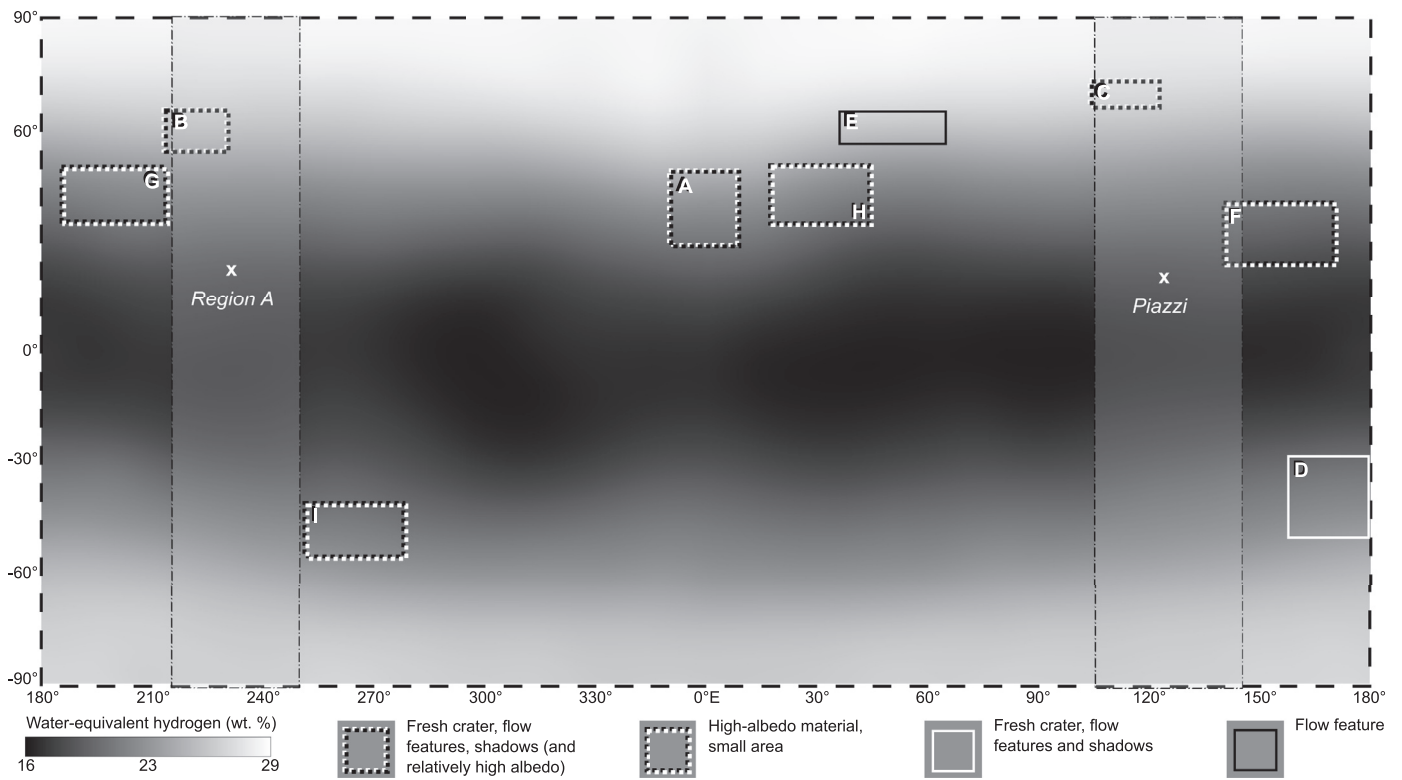


Fig. 16. Global distribution of water-equivalent hydrogen in the crust of Ceres from GRaND measurements (Prettyman et al., 2016) annotated with location of exposed H₂O-rich areas detected by VIR. The rectangles indicate the boundaries of FC context images, similar to Fig. 2, and the line style refer to the type of surface feature that is observed. The grey vertical bands and locations marked by an X labeled Region A and Piazz refer to the two areas identified as possible sources of H₂O vapor outgassing by Küppers et al. (2014). Projection: Simple Cylindrical; central meridian: 0.

telescope but not by Dawn, such as (24) Themis (Campins et al., 2010) and (65) Cybele (Licandro et al., 2011), Ceres offers the opportunity to make a comparison.

The latitude range of H₂O-rich areas identified by VIR (> 30°, North and South) is in contradiction with the values of 21°N and 23°N that resulted from modeling presented in Herschel observations. With VIR, the precision of the location is determined by the spatial resolution of the instrument. With Herschel, the latitude of H₂O outgassing reported in Küppers et al. (2014) was determined based on a model that is used to fit the observations. The uniqueness of this model is not well documented, and therefore there may be more than one latitude that could explain the observation for each site.

Within the two ranges of longitudes where H₂O outgassing was interpreted from Herschel observations (110°–145°E and 215°–250°E), exposed H₂O ice is detected by VIR, which might indicate a relationship between the two types of observation. However the large longitude ranges (35°) provided by Küppers et al. (2014) must be compared with the number (ten) of H₂O-rich sites detected by VIR globally (over 360° in longitude), which corresponds to an average longitude spacing of 36°. In VIR data, the two largest longitude ranges between two H₂O-rich areas are 95° and 60° respectively. As a result, assuming a random location of the 35°-large bands over Ceres, there is ~80% probability that one longitude range contains at least one local area of exposed H₂O ice detected by VIR, and ~70% probability that the two longitude ranges contain at least one H₂O-rich area observed by VIR. According to these numbers, the apparent agreement between the two observations is inconclusive: to date, it is not possible to relate the H₂O-rich areas observed by VIR with the H₂O outgassing regions reported by Küppers et al. (2014).

Finally, the total area of exposed H₂O ice by VIR is in the range of 10–20 km², whereas the outgassing surface calculated from

Herschel observations is 0.6 km². The difference in estimated area may be only an apparent discrepancy, because the two values correspond to different characteristics of the surface. Comparing the two numbers would imply that the entire area of exposed H₂O ice observed by VIR should be outgassing. In addition, the solar illumination – and thus the surface temperature – of any given H₂O-rich area varies throughout a cerean day due to the local topography, which may trigger sporadic outgassing. Consequently, on average, the outgassing area at any given time may be smaller than 1 km², even if the total H₂O-rich area is larger by one order of magnitude.

5. Conclusions

Absorption bands at 2.0 μm (and 1.65 and 1.28 μm) have been detected in VIR spectra at 9 different locations on Ceres, implying exposed H₂O-rich materials at the surface. Modeling of VIR spectra (e.g. Combe et al., 2016; Raponi et al., 2016) indicates H₂O ice as the component that most likely explains the H₂O detections in the spectra.

Each detection of H₂O absorption bands in the VIR spectra is associated with one or more distinctive surface features, such as a surface material with higher albedo than its surrounding terrains, or nearby a flow-like morphological feature observed at high resolution FC images. Three H₂O-rich areas have all these characteristics together, while the other six do not. Four of these sites are associated with persistent shadows. On the other hand, the observation of one or more distinctive surface features (high albedo, or flow-like feature, or persistent shadow) does not imply the detection of H₂O absorption bands in VIR spectra.

The spectral modeling of VIR spectra of H₂O-rich areas provides the best fit with H₂O ice, regardless of the technique used (intimate mixing by Raponi et al. (2016) based on the radiative transfer theory and the use of optical constants, or linear spectral

unmixing of laboratory spectra or modeled spectra combining different distributions of grain sizes presented in this study).

All H₂O absorption features are detected at latitudes above 30°, and correspond to areas of a few km² at maximum (three H₂O-rich areas associated with the Oxo crater cover a total of 6.8 km², and the northern wall of the Juling crater alone may represent about 6 km²). This distribution is consistent with temperature-dependent stability, which is expected for H₂O ice. Since H₂O ice in sunlit areas is short-lived on Ceres (Hayne and Aharonson, 2015; Formisano et al., 2016; Titus, 2015) at low latitude, these observations suggest that H₂O is present in the subsurface, the spectral detections imply that it has been recently exposed on the surface.

VIR detections of exposed H₂O at the surface of Ceres provide compelling evidence that H₂O ice is present in abundance in the subsurface, as originally suggested by low bulk density and modeling (McCord and Sotin, 2005), and now inferred from Dawn's observations of morphological flow-like features (Schmidt et al., 2017), interpretations of past cryovolcanism at Ahuna Mons (Ruesch et al., 2016; Nathues et al., 2017), the detection of excess elemental hydrogen in the crust (Prettyman et al., 2016), and models of the internal structure of Ceres from gravity and shape measurements (Park et al., 2016).

On Ceres, subsurface ice is ubiquitous (Prettyman et al., 2016), whereas exposed ice is rare. This finding has important implications for searching ice-rich small celestial bodies with Earth-based telescopes. As viewed from Earth or Earth-orbit, ice on the surface of main belt asteroids is rare, and even the Jovian Trojans appear to be mostly free of surface ice (Yang and Jewitt, 2007). Ceres is an example of an ice-rich body for which no detection of surface ice has been possible yet from Earth.

Acknowledgments

The funding for this research was provided under the NASA Dawn mission through a subcontract (2090-S-MB516) from the University of California, Los Angeles. The VIR instrument and VIR team are funded by ASI (Italian Space Agency) and INAF (Istituto Nazionale di Astrofisica).

References

- A'Hearn, M.F., Feldman, P.D., 1992. Water vaporization on Ceres. *Icarus* 98, 54–60.
- Acton C.H., 1996. Ancillary data services of NASA's navigation and ancillary information facility, planetary and space science, Volume 44, Issue 1, p. 65–70, doi: 10.1016/0032-0633(95)00107-7.
- Akimov, L.A., 1975. Influence of mesorelief on the brightness distribution over a planetary disk. *Astronomicheskii Zhurnal* 52 May-June 1975, p. 635–641 Soviet Astronomy, vol. 19, no. 3, 1976, p. 385–388 Translation.
- Ammannito, E., et al., 2016. The Distribution of Phyllosilicates on Ceres. *Science* 353.
- Campins, H., Hargrove, K., Pinilla-Alonso, N., Howel, E.S., Kelley, M.S., Licandro, J., Mothé-Diniz, T., Fernández, Y., Ziffer, J., 2010. Water ice and organics on the surface of the asteroid 24 Themis. *Nature* 464, 1320–1321. doi:10.1038/nature09029.
- Carrozzo, F.G., Raponi, A., Sanctis, M.C., Raponi, A., Ammannito, E., Giardino, M., D'Aversa, E., Fonte, S., Tosi, F., Capaccioni, F., Capria, M.T., Ciarniello, M., Longobardo, A., Palomba, E., Zambon, F., Russell, C.T., Raymond, C.A., 2016. Artefacts removal in VIR/DAWN data. *Rev. Sci. Instrum.* 87, 124501. <http://dx.doi.org/10.1063/1.4972256>.
- Castillo-Rogez, J., McCord, T.B., 2010. Ceres' evolution and present state constrained by shape data. *Icarus* 205, 443–459.
- Castillo-Rogez, J., Neveu, M., McSween, H., Fu, R., Toplis, M., Prettyman, T., 2018. *Meteor. Planet. Sci.* in press.
- Combe, J.-Ph., McCord, T.B., Tosi, F., Ammannito, E., Carrozzo, F.G., De Sanctis, M.C., Raponi, A., Byrne, S., Landis, M., Hughson, K.H.G., Raymond, C.A., Russell, C.T., 2016. Detection of local H₂O exposed at the surface of Ceres. *Science* 353 (6303). doi:10.1126/science.aaf3010.
- Combe, J.-Ph., et al., 2015. Reflectance properties and hydrated material distribution on Vesta: Global investigation of variations and their relationship using improved calibration of Dawn VIR mapping spectrometer. *Icarus* 259, 21–38.
- Combe, J.-P., et al., 2008. Analysis of OMEGA/Mars Express data hyperspectral data using a Multiple-Endmember Linear Spectral Unmixing Model (MELSUM): Methodology and first results. *Planet Space Sci* 56, 951–975.
- Combe, J.-Ph., Singh, S., Johnson, K.E., McCord, T.B., De Sanctis, M.C., Ammannito, E., Carrozzo, F.G., Ciarniello, M., Frigeri, A., Raponi, A., Tosi, F., Zambon, F., Scully, J., Raymond, C.A., Russell, C.T., 2018. The Surface Composition of Ceres' Ezinu quadrangle analyzed by the Dawn mission. *Icarus* this issue, in press.
- De Sanctis, M.C., et al., 2011. The VIR Spectrometer. *Space Sci. Rev* 163, 329–369.
- De Sanctis, M.C., Ammannito, E., Raponi, A., Marchi, S., McCord, T.B., McSween, H.Y., Capaccioni, F., Capria, M.T., Carrozzo, F.G., Ciarniello, M., Longobardo, A., Tosi, F., Fonte, S., Formisano, M., Frigeri, A., Giardino, M., Magni, G., Palomba, E., Turriani, D., Zambon, F., Combe, J.-P., Feldman, W., Jaumann, R., McFadden, L.A., Pieters, C.M., Prettyman, T., Toplis, M., Raymond, C.A., Russell, C.T., 2015. Ammoniated phyllosilicates with a likely outer Solar System origin on (1) Ceres. *Nature* 528 (7581), 241–244. doi:10.1038/nature16172.
- De Sanctis, M.C., Raponi, A., Ammannito, E., Ciarniello, M., Toplis, M.J., McSween, H.Y., Castillo-Rogez, J.C., Ehlmann, B.L., Carrozzo, F.G., Marchi, S., Tosi, F., Zambon, F., Capaccioni, F., Capria, M.T., Fonte, S., Formisano, M., Frigeri, A., Giardino, M., Longobardo, A., Magni, G., Palomba, E., McFadden, L.A., Pieters, C.M., Raymond, R., Schenk, P., Mugnuolo, R., Raymond, C.A., Russell, C.T., 2016. Bright carbonate deposits as evidence of aqueous alteration on (1) Ceres. *Nature* 536 (7614), 54–57. doi:10.1038/nature18290.
- Ermakov, A.I., Mazarico, E., Schroder, S.E., Carsenty, U., Schorghofer, N., Preusker, F., Raymond, C.A., Russell, C.T., Zuber, M.T., 2017. Ceres obliquity history and implications for the permanently shadowed regions. *Geophys. Res. Lett.* 44, 2652–2661. doi:10.1002/2016GL072250.
- Fanale, F.P., Salvail, J.R., 1989. The water regime of asteroid (1) Ceres. *Icarus* 82, 97–110. doi:10.1016/0019-1035(89)90026-2, ISSN 0019-1035.
- Filacchione, G., De Sanctis, M.C., Capaccioni, F., Raponi, A., Tosi, F., Ciarniello, M., Cerroni, P., Piccioni, G., Capria, M.T., Palomba, E., Bellucci, G., Erard, S., Bockeleer-Morvan, D., Leyrat, C., Arnold, G., Barucci, M.A., Fulchignoni, M., Schmitt, B., Quirico, E., Jaumann, R., Stephan, K., Longobardo, A., Mennella, V., Migliorini, A., Ammannito, E., Benkhoff, J., Bibring, J.P., Blanco, A., Blecka, M.L., Carlson, R., Carsenty, U., Colangeli, L., Combes, M., Combi, M., Crovisier, J., Drossart, P., Encrenaz, T., Federico, C., Fink, U., Fonti, S., Ip, W.H., Irwin, P., Kuehrt, E., Langevin, Y., Magni, G., McCord, T., Moroz, L., Mottola, S., Orofino, V., Schade, U., Taylor, F., Tiphene, D., Tozzi, G.P., Beck, P., Biver, N., Bonal, L., Combe, J.-P., Despan, D., Flamini, E., Formisano, M., Fornasier, S., Frigeri, A., Grassi, D., Gudipati, M.S., Kappel, D., Mancarella, F., Markus, K., Merlin, F., Orosei, R., Rinaldi, G., Cartacci, M., Cicchetti, A., Giuppi, S., Hello, Y., Henry, F., Jacquino, S., Reess, J.M., Noschese, R., Politi, R., Peter, G., 2016. Exposed water ice on the nucleus of comet 67P/Churyumov-Gerasimenko. *Nature* 529 (7586), 368–372. doi:10.1038/nature16190.
- Formisano, M., De Sanctis M.C., Magni G., Federico, C., Capria, M.T., 2016. Ceres water regime: surface temperature, water sublimation and transient exo(atmo)sphere. *Mont. Not. R. Astron. Soc.* 455, 1892–1904.
- Hapke, B., 1981. Bidirectional reflectance spectroscopy. I – Theory. *J. Geophys. Res.* 86, 3039–3054. doi:10.1029/JB086iB04p03039.
- Hayne, P.O., Aharonson, O., 2015. Thermal stability of ice on Ceres with rough topography. *J. Geophys. Res.* 120, 1567–1584.
- Hansen, G.B., 2009. Calculation of single-scattering albedos: comparison of Mie results with Hapke approximations. *Icarus* 203 (2), 672–676. doi:10.1016/j.icarus.2009.05.025.
- Küppers, M., et al., 2014. Localized sources of water vapour on the dwarf planet (1) Ceres. *Nature* 505 (7484), 525–527.
- Landis, M.E., Byrne, S., Schorghofer, N., Schmidt, B.E., Hayne, P.O., Castillo-Rogez, J., Sykes, M.V., Combe, J.-P., Ermakov, A.I., Prettyman, T.H., Raymond, C.A., Russell, C.T., 2017. Conditions for sublimating water ice to supply ceres' exosphere. *J. Geophys. Res. Planets* 122 (10), 1984–1995. doi:10.1002/2017JE005335.
- Lebofsky, L.A., Feierberg, M.A., Tokunaga, A.T., Larson, H.P., Johnson, J.R., 1981. The 1.7- to 4.2-micron spectrum of asteroid 1 Ceres - Evidence for structural water in clay minerals. *Icarus* 48, 453–459.
- Licandro, J., Campins, H., Kelley, M., Hargrove, K., Pinilla-Alonso, N., Cruikshank, D., Rivkin, A.S., Emery, J., 2011. (65) Cybele: detection of small silicate grains, water-ice, and organics. *Astron Astrophys* 525. doi:10.1051/0004-6361/201015339.
- Li, J.-Y., Reddy, V., Nathues, A., Le Corre, L., Izawa, M.R.M., Cloutis, E.A., Sykes, M.V., Carsenty, U., Castillo-Rogez, J.C., Hoffmann, M., Jaumann, R., Krohn, K., Mottola, S., Prettyman, T.H., Schaefer, M., Schenk, P., Schröder, S.E., Williams, D.A., Smith, D.E., Zuber, M.T., Konopliv, A.S., Park, R.S., Raymond, A., Russell, C.T., 2016. *Astrophys. J. Lett.* 817 (2), 7. doi:10.3847/2041-8205/817/2/L22, article id. L22.
- Longobardo, A., Palomba, E., De Sanctis, M.C., Ciarniello, M., Tosi, F., Carrozzo, F.G., Raponi, A., Zambon, F., Ammannito, E., Li, J.-Y., Raymond, C.A., Russell, C.T., 2016. Average photometric properties of ceres spectral parameters. In: *Proceedings of the 47th Lunar and Planetary Science Conference, held March 21-25, 2016 at The Woodlands, Texas, p. 2239. LPI Contribution No. 1903.*
- McCord, T.B., Sotin, C., 2005. Ceres: Evolution and current state. *J. Geophys. Res.* 110.
- Milliken, R.E., Rivkin, A.S., 2009. Brucite and carbonate assemblages from altered olivine-rich materials on Ceres. *Nat. Geosci.* 2, 258–261.
- Nathues, A., Hoffmann, M., Schaefer, M., Le Corre, L., Reddy, V., Platz, T., Cloutis, E.A., Christensen, U., Kneissl, T., Li, J.-Y., Mengel, K., Schmedemann, N., Schaefer, T., Russell, C.T., Applin, D.M., Buczkowski, D.L., Izawa, M.R.M., Keller, H.U., O'Brien, D.P., Pieters, C.M., Raymond, C.A., Ripken, J., Schenk, P.M., Schmidt, B.E., Sierks, H., Sykes, M.V., Thangjam, G.S., Vincent, J.-B., 2015. Sublimation in bright spots on (1) Ceres. *Nature* 528 (7581), 237–240. doi:10.1038/nature15754.
- Nathues, A., Hoffmann, M., Platz, T., Thangjam, G.S., Cloutis, E.A., Reddy, V., Le Corre, L., Li, J.-Y., Mengel, K., Rivkin, A., Applin, D.M., Schaefer, M., Christensen, U., Sierks, H., Ripken, J., Schmidt, B.E., Hiesinger, H., Sykes, M.V., Sizemore, H.G., Preusker, F., Russell, C.T., 2016. FC colour images of dwarf planet Ceres reveal a complicated geological history. *Planet. Space Sci.* 134, 122–127. doi:10.1016/j.pss.2016.10.017.

- Nathues, A., Platz, T., Hoffmann, M., Thangjam, G., Cloutis, E.A., Applin, D.M., Le Corre, L., Reddy, V., Mengel, K., Protospapa, S., Takir, D., Preusker, F., Schmidt, B.E., Russell, C.T., 2017. Oxo crater on (1) Ceres: geological history and the role of water-ice. *Astron. J.* 154. doi:[10.3847/1538-3881/aa7a04](https://doi.org/10.3847/1538-3881/aa7a04).
- Park, R.S., Konopliv, A.S., Bills, B.G., Rambaux, N., Castillo-Rogez, J.C., Raymond, C.A., Vaughan, A.T., Ermakov, A.I., Zuber, M.T., Fu, R.R., Toplis, M.J., Russell, C.T., Nathues, A., Preusker, F., 2016. A partially differentiated interior for (1) Ceres deduced from its gravity field and shape. *Nature* 537 (7621), 515–517. doi:[10.1038/nature18955](https://doi.org/10.1038/nature18955).
- Platz, T., Nathues, A., Schorghofer, N., Preusker, F., Mazarico, E., Schröder, S.E., Byrne, S., Kneissl, T., Schmedemann, N., Combe, J.-P., Schäfer, M., Thangjam, G.S., Hoffmann, M., Gutierrez-Marques, P., Landis, M.E., Dietrich, W., Ripken, J., Matz, K.-D., Russell, C.T., 2016. Surface water-ice deposits in the northern shadowed regions of Ceres. *Nat. Astron.* doi:[10.1038/s41550-016-0007](https://doi.org/10.1038/s41550-016-0007).
- Pieters, C.M., 1983. Strength of mineral absorption features in the transmitted component of near-infrared reflected light - First results from RELAB. *J. Geophys. Res.* 88, 9534–9544. doi:[10.1029/JB088iB11p09534](https://doi.org/10.1029/JB088iB11p09534), ISSN 0148-0227/Nov. 10, 1983.
- Prettyman, T.H., Yamashita, N., Castillo-Rogez, J.C., Feldman, W.C., Lawrence, D.J., McSween, H.Y., Schorghofer, N., Toplis, M.J., Forni, O., Joy, S.P., Marchi, S., Platz, T., Polansky, C.A., De Sanctis, M.C., Rayman, M.D., Raymond, C.A., Russell, C.T., 2016. Extensive water ice within Ceres' aqueously altered regolith: evidence from nuclear spectroscopy. *Science* 355, 55–59. doi:[10.1126/science.aah6765](https://doi.org/10.1126/science.aah6765).
- Raponi, A., Ciarniello, M., De Sanctis, M.C., Ammannito, E., Capaccioni, F., Capria, M.T., Carrozzo, F.G., Frigeri, A., Fonte, S., Giardino, M., Longobardo, A., Magni, G., Palomba, E., Tosi, F., Zambon, F., Raymond, C.A., Russell, C.T., 2016. Ceres spectral modelling with VIR data onboard Dawn: Method and first results. In: *Proceedings of the European Planetary Science Congress 2015, held 27 September - 2 October 2015 in Nantes, France*.
- Raponi, A., De Sanctis, M.C., Frigeri, A., Ammannito, E., Ciarniello, M., Formisano, M., Combe, J.-P., Magni, G., Tosi, F., Carrozzo, F.G., Fonte, S., Giardino, M., Joy, S.P., Polansky, C., Rayman, M.D., Capaccioni, F., Capria, M.T., Longobardo, A., Palomba, E., Zambon, F., Raymond, C.A., Russell, C.T., et al., 2018. Variations in the amount of water ice on Ceres' surface suggest a seasonal water cycle. *Sci. Adv.* in press.
- Rivkin, A.S., Volquardsen, E.L., Clark, B.E., 2006. The surface composition of Ceres: Discovery of carbonates and iron-rich clays. *Icarus* 185, 563–567.
- Roatsch, Th., et al., 2016. Ceres survey atlas derived from dawn framing camera images. *Planet. Space Sci.* 121, 115–120.
- Ruesch, O., et al., 2016. Cryovolcanism on Ceres. *Science* 353.
- Russell, C.T., Raymond, C.A., 2011. The Dawn mission to Vesta and Ceres. *Space Sci. Rev.* 163, 3–23.
- Schmidt, B.E., Hughson, K.H.G., Chilton, H.T., Scully, J.E.C., Platz, T., Nathues, A., Sizemore, H., Bland, M.T., Byrne, S., Marchi, S., O'Brien, D.P., Schorghofer, N., Hiesinger, H., Jaumann, R., Pasckert, J.H., Lawrence, J.D., Buzckowski, D., Castillo-Rogez, J., Sykes, M.V., Schenk, P.M., De Sanctis, M.C., Mitri, G., Formisano, M., Li, J.-Y., Reddy, V., Le Corre, L., Russell, C.T., Raymond, C.A., 2017. Geomorphological evidence for ground ice on dwarf planet Ceres. *Nat. Geosci.* 10 (5), 338–343. doi:[10.1038/ngeo2936](https://doi.org/10.1038/ngeo2936).
- Schröder, S.E., Mottola, S., Carsenty, U., Ciarniello, M., Jaumann, R., Li, J.-Y., Longobardo, A., Palmer, E., Pieters, C., Preusker, F., Raymond, C.A., Russell, C.T., 2017. Resolved spectrophotometric properties of the Ceres surface from dawn framing camera images. *Astrophys. - Earth Planet. Astrophys.* doi:[10.1016/j.icarus.2017.01.026](https://doi.org/10.1016/j.icarus.2017.01.026).
- Schorghofer, N., Mazarico, E., Platz, T., Preusker, F., Schröder, S.E., Raymond, C.A., Russell, C.T., 2016. The permanently shadowed regions of dwarf planet Ceres. *Geophys. Res. Lett.* 43, 6783–6789. doi:[10.1002/2016GL069368](https://doi.org/10.1002/2016GL069368).
- Schorghofer, N., 2016. Predictions of depth-to-ice on asteroids based on an asynchronous model of temperature, impact stirring, and ice loss. *Icarus* 276, 88–95.
- Shkuratov, Yu.G., Kreslavsky, M.A., Ovcharenko, A.A., Stankevich, D.G., Zubko, E.S., Pieters, C., Arnold, G., 1999. Opposition Effect from Clementine Data and Mechanisms of Backscatter. *Icarus* 141 (1), 132–155. doi:[10.1006/icar.1999.6154](https://doi.org/10.1006/icar.1999.6154).
- Thangjam, G., Hoffmann, M., Nathues, A., Li, J.-Y., Platz, T., 2016. Haze at Occator Crater on Dwarf Planet Ceres. *The Astrophys. J. Lett.* 833 (2), 9. doi:[10.3847/2041-8213/833/2/L25](https://doi.org/10.3847/2041-8213/833/2/L25), article id. L25.
- Thomas, P.C., et al., 2005. Differentiation of the asteroid Ceres as revealed by its shape. *Nature* 437, 224–226.
- Titus, T., 2015. Ceres: Predictions for near-surface water ice stability and implications for plume generating processes. *Geophys. Res. Lett.* 42, 2130–2136.
- Vernazza, P., et al., 2005. Analysis of near-IR spectra of 1 Ceres and 4 Vesta, targets of the Dawn mission. *Astron. & Astrophys.* 436, 1113–1121.
- Villarreal, M.N., Russell, C.T., Luhmann, J.G., Thompson, W.T., Prettyman, T.H., A'Hearn, M.F., Küppers, M., O'Rourke, L., Raymond, C.A., 2017. The dependence of the Cerean exosphere on solar energetic particle events. *The Astrophysical Journal Letters* 838, L8. doi:[10.3847/2041-8213/aa66cd](https://doi.org/10.3847/2041-8213/aa66cd).
- Xu, S., Binzel, R.P., Burbine, T.H., Bus, S.J., 1995. Small main-belt asteroid spectroscopic survey: Initial results. *Icarus* 115 (1), 1–35. doi:[10.1006/icar.1995.1075](https://doi.org/10.1006/icar.1995.1075), ISSN 0019-1035.
- Yang, B., Jewitt, D., 2007. Spectroscopic search for water ice on Jovian Trojan asteroids. *Astron. J.* 134 (1), 223.